AGU100 ADVANCING EARTH AND SPACE SCIENCE

Water Resources Research

RESEARCH ARTICLE
10.1029/2018WR023202

Key Points:
- Temporal evolution from heterotrophic to autolithotrophic denitrification for constant boundary conditions due to microbes preferring organic carbon
- Denitrification rates can drop significantly prior to total depletion of electron donors
- Nitrite may precede nitrate downstream of a nitrate source due to electron donor competition

Supporting Information:
- Supporting Information S1

Correspondence to:
D. Knabe,
dustin.knabe@tu-berlin.de

Citation:
Knabe, D., Kludt, C., Jacques, D., Lichtner, P., & Engelhardt, I. (2018). Development of a fully coupled biogeochemical reactive transport model to simulate microbial oxidation of organic carbon and pyrite under nitrate-reducing conditions. *Water Resources Research*, *54*, 9264–9286. https://doi.org/10.1029/2018WR023202

Received 25 APR 2018
Accepted 25 OCT 2018
Accepted article online 29 OCT 2018
Published online 23 NOV 2018

Development of a Fully Coupled Biogeochemical Reactive Transport Model to Simulate Microbial Oxidation of Organic Carbon and Pyrite Under Nitrate-Reducing Conditions

Dustin Knabe[1], Christoph Kludt[2,3], Diederik Jacques[4], Peter Lichtner[5,6], and Irina Engelhardt[1]

[1]Department of Hydrogeology, TU Berlin, Berlin, Germany, [2]Hessian Agency for Nature Conservation, Environment and Geology, Wiesbaden, Germany, [3]Hydrogeology Department, TU Darmstadt, Institute of Applied Geosciences, Darmstadt, Germany, [4]Institute for Environment, Health and Safety, Belgian Nuclear Research Centre (SCK•CEN), Mol, Belgium, [5]Center for Water and the Environment, University of New Mexico, Albuquerque, New Mexico, USA, [6]OFM Research Inc., Redmond, Washington, USA

Abstract In regions with intensive agriculture nitrate is one of the most relevant contaminants in groundwater. Denitrification reduces elevated nitrate concentrations in many aquifers, yet the denitrification potential is limited by the concentration of available electron donors. The aim of this work was to study the denitrification potential and its limitation in natural sediments. A column experiment was conducted using sediments with elevated concentrations of organic carbon (total organic carbon 3,247 mg C/kg) and pyrite (chromium reducible sulfur 150 mg/kg). Groundwater with high nitrate concentration (100 mg/L) was injected. Measurements were taken over 160 days at five different depths including N- and S-isotope analysis for selected samples. A reactive transport model was developed, which couples nitrate reduction with the oxidation of organic carbon (heterotrophic denitrification) and pyrite (autolithotrophic denitrification), and considers also transport and growth of denitrifying microbes. The denitrification pathway showed a temporal sequence from initially heterotrophic to autolithotrophic. However, maximum rates were lower for heterotrophic (11 mmol N/(L*a)) than for autolithotrophic denitrification (48 mmol N/(L*a)). The modeling showed that denitrifying microbes initially preferred highly reactive organic carbon as the electron donor for denitrification but were also able to utilize pyrite. The results show that after 160 days nitrate increased again to 50 mg/L. At this time only 0.5% of the total organic carbon and 46% of the available pyrite was oxidized. This indicates that denitrification rates strongly decrease before the electron donors are depleted either by a low reactivity (total organic carbon) or a diminishing reactive surface possibly due to the presence of coatings (pyrite).

1. Introduction

In intensively used agricultural areas nitrogen-based fertilizers have been applied now for decades with the aim to raise soil productivity. Significant amounts of nitrate can reach underlying aquifers due to leaching through the soil and unsaturated zone, and thus can have negative effects for drinking water quality (Böhlke, 2002; Böttcher & Strebel, 1987; Liao et al., 2012). Much effort has been dedicated in Germany to improve the chemical status of the groundwater bodies in accordance with the EU Water Framework Directive 2000/60/EC. However, investigations conducted in 2012–2014 showed that 28% of the aquifers still contain nitrate concentrations above the Environmental Quality Standard of the Water Framework Directive of 50 mg/L (BMUB and BMEL, 2016).

Denitrification reduces nitrate to N_2 with intermediate production of nitrite and gases like NO and N_2O. It occurs under anaerobic conditions as respiratory process and reduces oxidized forms of nitrogen in response to the oxidation of an electron donor. Denitrification is controlled by the availability of adequate reactive electron donors (Hiscock et al., 1991; Kölle, 1984; Postma et al., 1991; Rohmann & Sontheimer, 1985; Smith & Duff, 1988; Wisotzky et al., 2011; Zhang et al., 2009). If heterotrophic (hetero-chemoorganotrophic) denitrification occurs, organic carbon (C_{org}) acts as the electron donor (Bradley et al., 1992; Bragan et al., 1997; Smith et al., 1996; Starr & Gillham, 1993; Trudell et al., 1986). If autolithotrophic denitrification occurs, sulfide mineral phases, such as pyrite (FeS_2), act as electron donors (Kölle et al., 1983; Postma et al., 1991;

Robertson et al., 1996; Strebel et al., 1985; Tesoriero et al., 2000). Furthermore, nitrate reduction by oxidation of Fe(II)-rich clay minerals, such as smectite (Ernstsen, 1996; Hofstetter et al., 2002), Fe(II)-rich amphibole and pyroxenes (Postma, 1990), and Fe(II),(III)-oxides/-hydroxides, such as magnetite or green rust (Hansen & Koch, 1998), has been observed in experimental studies.

In general, the energy yield of heterotrophic denitrification is higher than for autolithotrophic denitrification (Stumm & Morgan, 1996; Wagman, 1982). However, Postma et al. (1991) proposed that in sandy aquifers and under conditions with high total organic carbon (TOC) content (up to 3,600 mg C/kg) and low sulfide content (230 up to 960 mg S/kg sulfide), autolithotrophic denitrification might be the relevant process for denitrification. Pätsch (2006) and Konrad (2006) also observed that for microbial denitrification sulfides served as the favored electron donor compared to organic carbon in sedimentary aquifers. This was explained by the low reactivity of the organic carbon in sediments, which mainly consist of wood residue. Therefore, not only the total concentration of organic carbon but also its reactivity is the key factor to determine the relevant denitrification process and rates. In addition, Böhlke et al. (2002) showed based on isotopic data that FeS_2 and other Fe(II) phases act as major electron donors for denitrification. However, Tesoriero and Puckett (2011) reported the highest denitrification rates if both electron donors, sulfide and organic carbon, are present. These results demonstrate that although the reaction pathways of these denitrification processes are well known, the kinetics of the reactions as well as the competition between the various processes involved are still uncertain.

Currently, concentrations of SO_4^{2-}, Fe^{2+}, and HCO_3^- along the groundwater flow path and redoxcline are used as indicators for heterotrophic or autolithotrophic denitrification (Postma et al., 1991; Tesoriero et al., 2000). However, other geochemical reactions within the aquifer can provide additional sources and sinks for these species along the flow path, e.g., dissolution of calcite or gypsum. Thus, using concentrations of redox species as stand-alone indicators might result in erroneous conclusions. A well-established approach to identify nitrate and sulfate sources and reduction rates is the comparison between the reactants and products of stable isotope ratios of oxygen, nitrogen, and sulfur ($^{15}N/^{14}N$, $^{34}S/^{32}S$, $^{18}O/^{16}O$; Aravena & Robertson, 1998; Groffman et al., 2009). Aravena and Robertson (1998) used multiple isotope tracers, including sulfur isotopes, to identify denitrification and to evaluate the importance of different electron donors. Knöller et al. (2005) highlight that if the isotopic composition of the sulfur sources is known, the $^{34}S/^{32}S$ isotopic ratio can be used to identify sulfur sources and the existence of sulfide oxidation from autolithotrophic denitrification. This is possible since isotopic fractionation and thus isotopic enrichment does not occur during sulfide oxidation (Seal, 2006; Vaughan, 2006), resulting in sulfate with an "isotopic fingerprint" of the sulfide (e.g., pyrite). In contrast to sulfide oxidation, isotopic fractionation occurs during nitrate reduction and reveals the reduction rate as well as the activity of the microbial population (Frey et al., 2014; Knöller et al., 2011; Wunderlich et al., 2012). Therefore, using a dual-isotope approach is a valuable tool to use information about nitrate and sulfate sources to identify the key processes for denitrification (Knöller et al., 2011). Recent studies (Böhlke et al., 2002; Strebel et al., 1992; Tesoriero & Puckett, 2011; Tesoriero et al., 2000; Zhang et al., 2012, 2009) show that at field scale, the overall denitrification rates can be also determined by $N_{2Excess}$ using the N_2/Ar method.

A further suitable way to analyze denitrification processes is the use of reactive transport simulations. Current numerical investigations of denitrification processes simulate nitrate reduction by organic carbon degradation based on the Monod approach. Some of those models do not consider in detail microbial growth (Antoniou et al., 2013; Engelhardt et al., 2014), while others account for microbial growth and decay (Clement et al., 1997; Rodríguez-Escales et al., 2016). Some investigations are based on laboratory studies (Clement et al., 1997; Mastrocicco et al., 2011; Molins et al., 2015; Rodríguez-Escales et al., 2016), while others analyze field investigations (Engelhardt et al., 2014; Lee et al., 2009). A special case is the thermodynamic approach which was employed by André et al. (2011) for their laboratory studies using thermodynamic factors similar to Monod factors and which account for changes in the thermodynamic equilibrium of the redox reaction. Maggi et al. (2008) included reactions for all intermediate N species in a field-scale modeling also including the growth of microorganisms. Arora et al. (2016) modeled field-scale heterotrophic denitrification and autolithotrophic denitrification with Fe^{2+} and HS^-. Different reaction rates for N and O isotopes in nitrate were included by Lehmann et al. (2003). Pyrite oxidation was simulated at the field scale with a partly empiric approach considering the concentration of pyrite, nitrate, and the pH value (Eckert & Appelo, 2002; Prommer

& Stuyfzand, 2005). However, current published research does not consider (i) the effects of microbial growth and death cycles for autolithotrophic denitrification, (ii) competitive oxidation of organic carbon and pyrite, and often (iii) the transport of microorganisms is disregarded.

Denitrification irreversibly consumes electron donors, for example, sulfides and organic carbon (Kölle et al., 1983; Strebel et al., 1992). Recent field investigations indicate increasing nitrate concentrations in drinking water that might result from the depletion of the electron donors, and thus the denitrification capacity of the aquifer (Bergmann et al., 2013; Hansen et al., 2011). However, the concentration, surface area, and spatial distribution of the electron donors and kinetic reactive phases, for example, sulfides and organic carbon, in the aquifer systems, are typically not known in detail and difficult to measure at the field scale. Therefore, field-scale estimation of degradation rates and the prediction of field-scale, long-term denitrification capacity still remain difficult. It continues to be an important task for current and future research to improve our understanding about how long-term denitrification rates are affected by the availability and the spatial distribution of different electron donors. Our research focuses on the numerical analysis of laboratory column experiments with sediments collected from an aquifer in a region intensively used for agricultural purposes and strongly affected by groundwater with high nitrate concentrations to (i) identify key processes driving denitrification in natural sediments, (ii) to provide parameter sensitivities and uncertainties employed in the biogeochemical model, (iii) to assess the worth of additional isotopic measurements to characterize the denitrification pathways, and (iv) to provide insight into denitrification during progressive depletion of natural electron donors.

2. Materials and Methods

2.1. Laboratory Experiment

2.1.1. Field Site, Investigated Aquifer, and Sediments

Sediment samples were taken from the Hessian Ried (1,200 km^2) that is located in the northern part of the Rhine Graben, Germany. The sedimentary aquifer, which was investigated, consists of Quaternary permeable sand and gravel layers separated by silt, clay, or silty fine sand layers. Sediment samples were taken from a borehole drilled within a small forest surrounded by agricultural fields. For the sample collection a borehole was drilled using the inliner drilling method down to a depth of up to 60 m. The sediments in general consist mainly of sandy to silty Quaternary eolian deposits.

The sediment samples for the column experiments are from a horizon of about 1.5-m thickness in 25-m depth, which is characterized by a high portion of fine content (silt and clay $>$40%, fine sand $>$40%), a high carbonate content (total inorganic carbon = 33 g/kg), and a dark gray brown color. The horizon corresponds to a low permeable layer, which separates the aquifer into an upper (oxic, higher nitrate content) and a lower (anoxic, lower nitrate content) part. The layer was chosen due to its high organic carbon (3247 mg C/kg) and sulfide (150 mg S/kg) content.

Collected sediment samples were immediately stored in airtight PE-Al-composite bags under N_2-gas atmosphere. Samples were then frozen, freeze-dried, and stored at room temperature in the dark. Prior to laboratory analyses sediment samples were milled and pressed into pellets with a binder (Hoechst Wachs C, Merck KGaA, Darmstadt, Germany) using a mass ratio of 4:1.

The content of total organic carbon (TOC) and inorganic carbon of the sediment was measured by sequential combustion (Liqui TOC II, Elementar Analysensysteme GmbH, Hanau, Germany). The total elemental composition including total sulfur was measured using wavelength dispersive X-ray fluorescence (AXS S8 Tiger 1K, Bruker GmbH, Karlsruhe, Germany). The contents of sulfide and disulfide phases were quantified by the chromium reducible sulfur (CRS) method (Canfield et al., 1986; van der Veen, 2003), according to DIN51724–2 (1999).

TOC, wavelength dispersive X-ray fluorescence, and CRS methods were validated with synthetic sediment samples prepared from acid-washed quartz sand and by adding varying amounts of elemental and organic carbon, elemental sulfur, organic sulfur (cysteine; Carl Roth GmbH & Co. KG, Karlsruhe, Germany), and pyrite (FeS_2; Alfa Aesar GmbH & Co. KG, Karlsruhe, Germany). The validation was conducted to determine the limits of quantification for pyrite using the CRS method (18 mg S/kg) and for TOC using the sequential combustion method (90 mg C/kg).

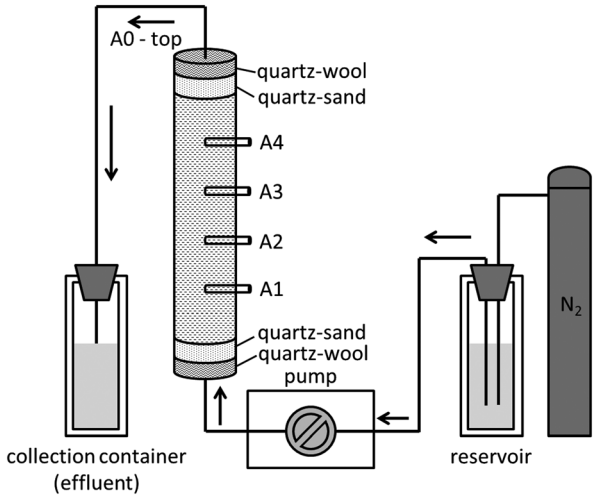

Figure 1. Experimental setup, location of the sampling ports A1–4, and the outflow A0.

2.1.2. Laboratory Column Experiments

Laboratory column experiments were conducted with Plexiglas tubes (wall thickness of 5 mm) with a length of 51.5 cm, an inside diameter of 5 cm, and Plexiglas plates at the top and bottom of the column with a thickness of 1.5 mm. Packing of the sediments was conducted according to DIN19528 (2009) to ensure a homogeneously packed column. In addition, the column was wrapped in aluminum foil to protect the sediment from contact with light to prevent algal growth. On the top and bottom of the aquifer sediment sample a 0.5-cm layer of quartz-wool and a 2-cm quartz-sand layer was added to ensure a homogenous flow direction.

Water samples were collected at the outlet (A0) at the top of the column and at four further sampling ports that were installed along the column (A1 to A4) separated by a distance of 10 cm (Figure 1). Ports A1 to A4 consisted of suction cups (ecoTech, Bonn, Germany) made of a porous polymer tube with a pore diameter of 0.15 μm. A combination of circular sealing rings, Teflon tape (PTFE), and self-sealing tape was used to seal the column at the inlet and outlet and sampling ports. Water samples were collected in burette bottles.

Water was injected with a multichannel peristaltic pump (MS/CA8–6) at the bottom of the column applying a constant flow rate of 0.031 mL/min. This flow rate equals the mean flow velocity in the Hessian Ried and allowed for sufficient contact time between the pore water solutes and the sediment. An upward flow direction was applied to minimize negative effects of air inclusions, sidewall leakage, and preferential flow paths or the blocking of flow channels by gas formation (Pätsch, 2006). Water samples along the column were taken with Tygon® standard tubing with 0.38- and 0.51-mm internal diameter and Tygon® "two-stop tubing" with an internal diameter of 0.64 mm (ISMATEC/IDEX Health & Science GmbH, Wertheim, Germany).

Before the start of the experiment the column was filled with carbon dioxide gas over a period of 2 hr to displace atmospheric air from the pore space. Due to the higher solubility of gaseous CO_2 compared to atmospheric air in water a very high saturation with water was achieved with this method and oxygen was displaced from the pore space.

In the next step an initial saturation with deionized water containing 50 mg/L NaCl and 125 mg/L of $MgSO_4{\cdot}7H_2O$ was established.

After 37 days, during which 4.6 L of deionized water was applied (8.6 pore volumes) under fully saturated conditions, geochemical equilibrium was achieved as indicated by constant hydraulic and chemical parameters at the outflow. Then nitrate-enriched synthetic groundwater was added. The composition of the synthetic groundwater equaled the typical groundwater composition in the Hessian Ried containing 50 mg/L of sodium chloride (NaCl) and 125 mg/L of magnesium sulfate ($MgSO_4{\cdot}7H_2O$). The synthetic groundwater was enriched with 200 mg/L Ca $(NO_3)_2{\cdot}4H_2O$, which resulted in nitrate concentrations of approximately 100 mg NO_3^-/L. Finally, the column was purged with nitrogen 5.0 (purity: 99.999%) to produce anaerobic conditions.

A conservative tracer test with bromide was performed to determine the transport parameters (effective porosity, dispersivity) of the sediment. For this purpose, a sodium bromide solution was added to the nitrate-enriched synthetic groundwater to produce a tracer pulse with a constant bromide concentration of 10 mg/L.

Water samples were taken at the outlet every two to three days and at sampling ports A1 to A4 once a week. At each port a maximum water volume of 6.5 mL was taken out simultaneously from the column using a uniform pump rate of 0.031 mL/min. To maintain fully saturated conditions during the sampling the pumping rate was increased to prevent unsaturated conditions and to reduce the risk of changes in the flow pattern.

Major ions (Li^+, Na^+, NH_4^+, Mg^{2+}, Ca^{2+}, F^-, Cl^-, NO_2^-, Br^-, NO_3^-, PO_4^{3-}, SO_4^{2-}) of the water samples were analyzed using ion chromatography (882 Compact IC plus, Metrohm, Germany) with a Metrosep C4–25/4.0

column for cations and a Metrosep A Supp 5 250/4.0 column for anions. Hydrogen carbonate (HCO_3^-) was measured with titration using 10 mL samples, 0.1 N HCl, Methyl orange as indicator, and a Dosimat 665 (Methrom AG, Herisau). The iron and manganese concentrations were measured by atomic absorption spectrometry using a ContrAA 300 (Analytik Jena, Jena). Standards with concentrations of 0.5, 1, 5, 10, 15, 20, 25, and 30 mg/L were used for calibration.

2.1.3. Isotopic Analyses of Water and Sediment Samples

Sulfur isotopes within the water samples were analyzed using sulfate, which was extracted as $BaSO_4$ by adding $BaCl_2$. The sulfide, disulfide, and elemental sulfur were extracted from the sediment samples using the CRS method. For this, acidified $CrCl_2$ solution was added and the sediment sample was boiled over 2 h (Canfield et al., 1986; Fossing & Jørgensen, 1989). Resulting H_2S was transferred by a N_2 gas flow into a zinc acetate trap, precipitated as ZnS, and was then converted to Ag_2S by addition of 0.1 M $AgNO_3$ solution. $BaSO_4$ or Ag_2S was transferred to SO_2 using a continuous flow combustion technique coupled with isotope-ratio mass spectrometry (delta S, Thermo Scientific, USA). Sulfur isotope signatures are reported in δ notation ($\delta^{34}S$) as parts per thousand (‰) deviation relative to the Vienna Canon Diablo Troilite (VCDT) standard. The overall analytical precision for sulfur isotope measurements was ±0.4‰. For normalizing the $\delta^{34}S$ data, the reference materials NBS 127 ($BaSO_4$; 20.3‰ VCDT) and IAEA-S1 (Ag_2S; 0.3‰ VCDT) were used.

Oxygen isotope analysis of $BaSO_4$ samples was conducted with high-temperature pyrolysis at 1,450 °C in a TC/EA that was connected to an isotope-ratio mass spectrometer (delta S, Thermo Scientific, USA) resulting in an analytical precision of ±0.5‰. The results of oxygen isotope measurements are expressed in δ notation ($\delta^{18}O$) as parts per thousand (‰) deviation relative to Vienna Standard Mean Ocean Water. The normalization of oxygen isotope data of sulfate was carried out using the reference material NBS-127 $BaSO_4$ with an assigned $\delta^{18}O$ value of 8.6‰ (Vienna Standard Mean Ocean Water).

Nitrogen isotopic analysis of nitrate, expressed in δ notation relative to the standard air, was measured by the denitrifier method (Gasbench II/delta V plus combination, Thermo Scientific, USA). $\delta^{15}N$ was determined from N_2O produced by a controlled reduction of nitrate within the sample (Casciotti et al., 2002; Sigman et al., 2001). For calibration of nitrogen isotope values, the reference materials IAEA-N3 ($\delta^{15}N$: +4.7‰ AIR), USGS32 ($\delta^{15}N$: +180‰ AIR), USGS 34 ($\delta^{15}N$: −1.8‰ AIR), and USGS 35 ($\delta^{15}N$: +2.7‰ AIR) were used. The analytical precision of the denitrifier method for $\delta^{15}N$ was ±0.4‰.

2.2. Numerical Investigations

Numerical investigations were carried out with the code HP1 (Jacques et al., 2018), which is a numerical solver for multicomponent reactive transport for variably saturated water flow conditions. It couples HYDRUS-1D (Šimůnek et al., 2016) for solving the Richards equation and the advection-dispersion equation with PHREEQC (Parkhurst & Appelo, 2013) for solving the biogeochemical processes to simulate multicomponent reactive transport in variable saturated porous media. Our simulations used the HP1 code with the standard "phreeqc.dat" database but with the nitrate-nitrite equilibrium speciation disabled as nitrite accumulated kinetically in our experiment.

2.2.1. Simulation of Water Flow and Conservative Transport

The laboratory column of 51.5-cm length was discretized into 115 nodes with equal spacing. The model column includes the filter (2.5 cm on each side) and sediment material (46.5 cm). Both materials used the same hydraulic conductivity, porosity, and dispersivity as the filter porosity is unknown and test simulations showed that the porosity error introduced by this approach is negligible.

Hydraulic conductivities of the aquifer sediment and filters equal 3.5×10^{-5} m/s. Constant flux boundaries were applied at the inflow and outflow boundary, and thus, the hydraulic conductivity did not influence the flow velocity and is therefore of less importance for our investigation. Conservative transport parameters (porosity and dispersivity) were calibrated with the bromide tracer breakthrough curve.

2.2.2. Governing Equations for Microbial Nitrate Reduction

Key processes in our reactive transport model include (i) growth and decay of microorganisms; (ii) attachment and detachment of microorganisms to the soil surface, having a mobile (suspended in the water phase) and immobile (attached to the soil) pool of microorganisms; (iii) both heterotrophic (oxidation of sedimentary organic carbon (SOC)) and autolithotrophic (oxidation of pyrite) microbial denitrification processes (Bosch et al., 2011; Strohm et al., 2007; Torrentó et al., 2011); and (iv) advection, diffusion, and dispersion of

mobile microorganisms and solutes. Nitrate and nitrite are measured and accounted for in the simulations to replicate reduction of nitrate to nitrite (step (a)) and reduction of nitrite to N_2 (step (b)).

2.2.2.1. Microbial Growth and Transport of Microorganism

The rate of change of attached and detached microbe concentrations are described as

$$r_{a,micr} = -k_{att}\cdot c_{s.micr} + k_{det}\cdot c_{a,micr} + d\cdot c_{a,micr} - \left(y_{SOC}\cdot r_{SOC} + y_{pyr}\cdot r_{pyr}\right) \quad (1)$$

$$r_{s,micr} = +k_{att}\cdot c_{s.micr} - k_{det}\cdot c_{a,micr} + d\cdot c_{s,micr} \quad (2)$$

where $r_{a/s,micr}$ is the rate of the microbe concentration change for the microbes attached to the sediment (index a) and suspended in the water phase (index s; mol-cells·L^{-1}·day^{-1}) expressed as negative of the time derivative of the concentration, k_{att} and k_{det} are the constant attachment and detachment coefficients (day^{-1}), d is the decay coefficient (day^{-1}), $y_{SOC/pyr}$ are the microbial yield factors for oxidation of SOC and pyrite (mol-cells mol^{-1}), $r_{SOC/pyr}$ are the oxidation rates of SOC and pyrite (mol L^{-1} day^{-1}), $c_{s,micr}$ is the concentration of mobile microbes suspended in the water phase (mol-cells L^{-1}), and $c_{a,micr}$ is the microbe concentration attached to the sediment, that is for simplification expressed in mol-cells per liter solute volume.

In this conceptual model, we assumed that only attached microbes are directly affected by growth as only electron donors in the solid phase are considered with DOC being negligible (the growth term is only present in equation (1), the fourth term). We observed in our experiment a temporal sequence of heterotrophic and autolithotrophic denitrification. The simulations consider that the microbes are autolithotrophic if the concentration of reactive organic carbon is very low (only one microbial population is considered for both denitrification processes). Growth (fourth term of equation (1)) and decay (third term in equations (1) and (2)) are simulated similar to the studies of Lee et al. (2009) and Rodríguez-Escales et al. (2016). Many approaches have been published to simulate microbial transport that account for the attachment and detachment of microbes to and from the sediment (Tufenkji, 2007). The simplest approach to consider microbial transport is first-order attachment and detachment with constant coefficients as, that is, in Clement et al. (1997) (the first two terms of equations (1) and (2)).

More complex approaches for microbial transport like colloid filtration theory (Ginn et al., 2002) include the median grain size, colloid/microbe size, particle velocity, porosity, and saturation. Also known to be relevant for colloid transport are pH and ionic strength especially through their influence on the electrostatic double layer (Ginn et al., 2002). Most of these variables are constant under the experimental conditions; only ionic strength increases from about 4.5 to 6.0 mmol/L during the experiment. Therefore, the implemented approach can be expected to reproduce the microbial transport reasonably well under the prevailing geochemical conditions.

The microbe concentrations are normalized to the initial concentration of attached microbes to avoid assuming an absolute value of the initial concentration in the absence of measurements (see also section 2.2.3):

$$\frac{c_{a,micr}(x,t)}{c_{a,micr}(x,t=0)} = \frac{c_{a,micr}(x,t)}{c_{a,micr,0}} = c_{a,\mathrm{norm}}(x,t) \quad (3)$$

where $c_{a,norm}(x, t)$ is the normalized (dimensionless) concentration of attached microbes at distance x and time t. The normalized concentration of attached microbes is therefore 1 at the start of the model calculations.

The geochemical rate for the normalized attached microbes can be formulated as

$$r_{a,\mathrm{norm}} = -k_{att}\cdot c_{s,\mathrm{norm}} + k_{det}\cdot c_{a,\mathrm{norm}} + d\cdot c_{a,\mathrm{norm}} - \left(Y_{SOC}\cdot r_{SOC} + Y_{pyr}\cdot r_{pyr}\right) \quad (4)$$

where $Y_i\left(=\frac{y_i}{c_{a,micr,0}}\right)$ is the normalized growth yield (L/mol) for the oxidation of species i.

Similarly, equation (4) for suspended microbes can be written as

$$r_{s,\mathrm{norm}} = k_{att}\cdot c_{s,\mathrm{norm}} - k_{det}\cdot c_{a,\mathrm{norm}} + d\cdot c_{s,\mathrm{norm}} \quad (5)$$

2.2.2.2. SOC Degradation

Heterotrophic denitrification is based on the degradation of dissolved and sediment-bound organic carbon (DOC and SOC). The inflowing artificial groundwater was free of DOC; therefore, transport of DOC is disregarded in the simulations. Degradation of SOC is described with the following geochemical reactions:

$$C_{org} + 2\,NO_3^- + H_2O \rightarrow 2\,NO_2^- + HCO_3^- + H^+ \tag{6}$$

$$3\,C_{org} + 4\,NO_2^- + H_2O + H^+ \rightarrow 2\,N_2 + 3\,HCO_3^- \tag{7}$$

Oxidation of SOC can be described using Monod kinetics, where the oxidation rate is linearly coupled with the microbial mass and limited by the electron donor (SOC) and acceptor (nitrate and nitrite) availability.

For both denitrification steps, (a) and (b), the denitrification rates are formulated with

$$r_{SOC,a} = k_{m,SOC,a} \cdot c_{a,micr} \cdot \frac{c_{SOC}}{c_{SOC} + k_{SOC,a}} \cdot \frac{c_{NO_3^-}}{c_{NO_3^-} + k_{NO_3^-}} \tag{8}$$

$$r_{SOC,b} = k_{m,SOC,b} \cdot c_{a,micr} \cdot \frac{c_{SOC}}{c_{SOC} + k_{SOC,b}} \cdot \frac{c_{NO_2^-}}{c_{NO_2^-} + k_{NO_2^-}} \tag{9}$$

where $k_{m,SOC,a/b}$ are the specific rate constants for steps (a) and (b), respectively (mol-SOC·mol-cells^{-1}·day^{-1}); $c_{a,micr}$ is the concentration of attached microbes (mol-cells·L^{-1}); c_{SOC} is the sediment organic carbon concentration with respect to solute volume (mol/L); $k_{SOC,a/b}$ is the organic carbon half-saturation constant (mol/L); $c_{NO3-/NO2-}$ are the nitrate and nitrite concentrations (mol/L); and $k_{NO3-/NO2-}$ are the nitrate and nitrite half-saturation constants (mol/L).

Considering the normalized microbe concentrations, the denitrification rates are

$$r_{SOC,a} = k_{m,SOC,a} \cdot c_{a,micr} \cdot \frac{c_{SOC}}{c_{SOC} + k_{SOC,a}} \cdot \frac{c_{NO_3^-}}{c_{NO_3^-} + k_{NO_3^-}} = \\ = K_{m,SOC,a} \cdot c_{a,\mathrm{norm}} \cdot \frac{c_{SOC}}{c_{SOC} + k_{SOC,a}} \cdot \frac{c_{NO_3^-}}{c_{NO_3^-} + k_{NO_3^-}} \tag{10}$$

and for reaction step (b):

$$r_{SOC,b} = k_{m,SOC,b} \cdot c_{a,micr} \cdot \frac{c_{SOC}}{c_{SOC} + k_{SOC,a}} \cdot \frac{c_{NO_2^-}}{c_{NO_2^-} + k_{NO_2^-}} = \\ = K_{m,SOC,b} \cdot c_{a,\mathrm{norm}} \cdot \frac{c_{SOC}}{c_{SOC} + k_{SOC,b}} \cdot \frac{c_{NO_2^-}}{c_{NO_2^-} + k_{NO_2^-}} \tag{11}$$

where $K_{m,SOC,a/b}$ ($=k_{m,\,SOC,\,a/b} \cdot c_{a,\,micr,\,0}$) are the normalized rate constants for steps (a) and (b) (mol·L^{-1}·day^{-1}), and $c_{a,norm}$ is the normalized concentration of attached microbes.

2.2.2.3. Pyrite Oxidation

Autolithotrophic denitrification based on the oxidation of pyrite is often assumed to include the oxidation of iron(II) to iron(III), which then precipitates as iron(III)-hydroxide (Prommer & Stuyfzand, 2005). The geochemical equation of Prommer and Stuyfzand (2005) is adapted to the two-step approach of this study:

$$\text{(a)}\ 2\,FeS_2 + 15\,NO_3^- + 7\,H_2O \rightarrow 15\,NO_2^- + 4\,SO_4^{2-} + 2\,Fe(OH)_3 + 8\,H^+ \tag{12}$$

$$\text{(b)}\ 2\,FeS_2 + 10\,NO_2^- + 2H_2O + 2\,H^+ \rightarrow 5\,N_2 + 4\,SO_4^{2-} + 2\,Fe(OH)_3 \tag{13}$$

An empirical equation for the oxidation rate of pyrite due to reduction of oxygen and nitrate was published by Eckert and Appelo (2002) and Prommer and Stuyfzand (2005), who based their research on the previous work of Williamson and Rimstidt (1994) and Appelo et al. (1998). Oxygen was not present in our experiment and the calculation of the pyrite oxidation rate is therefore reduced to

$$r_{pyr} = c_{NO_3^-}^{p_2} \cdot c_{H^+}^{p_3} \cdot \left(k_{pyr} \cdot p_4 \cdot c_{pyr,0}\right) \cdot \left(\frac{c_{pyr}}{c_{pyr,0}}\right)^{2/3} \tag{14}$$

where r_{pyr} is the rate of pyrite oxidation (mol·L^{-1}·day^{-1}); c_{NO3^-,H^+} are the concentrations of nitrate and hydrogen (mol/L); k_{pyr} is the specific rate constant (dm·mol·L^{-1}·day^{-1}), which was originally determined by Williamson and Rimstidt (1994) with 5.58×10^{-6} (dm·mol·L^{-1}·day^{-1}); c_{pyr} is the current pyrite concentration (mol/L); $c_{pyr,0}$ is the initial pyrite concentration (mol/L); and $p_{2,3}$ are the exponent parameters. The parameters p_2 and p_3 were originally determined by Williamson and Rimstidt (1994) with values of 0.5 and −0.11, respectively, derived from the oxidation of pyrite from oxygen respiration, but were later also used for nitrate reduction by Eckert and Appelo (2002) and Prommer and Stuyfzand (2005). The parameter p_4 is the initial pyrite surface area per mole of pyrite (dm^2/mol). The last term of equation (14) assumes that the pyrite minerals dissolve like an ideal cube/sphere and that the number of pyrite grains per unit volume remains fixed (Appelo et al., 1998). The surface area therefore decreases with a power of 2/3 with decreasing pyrite concentration.

For simulation of autolithotrophic nitrate reduction, the oxidation rate of pyrite as given in Prommer and Stuyfzand (2005) is coupled with the microbial concentration to include microbial growth and its impact on the reaction. The pyrite oxidation rate was calculated for step (a) with

$$r_{pyr,a} = \left\{ c_{NO_3^-}^{p_2} \cdot c_{H^+}^{p_3} \cdot \left(k^*_{pyr,a} \cdot p_4 \cdot c_{pyr,0} \right) \cdot \left(\frac{c_{pyr}}{c_{pyr,0}} \right)^{2/3} \right\} \cdot c_{a,\mathrm{norm}} \cdot Z(c_{SOC}) \tag{15}$$

where

$$Z(c_{SOC}) = \begin{cases} 0, c_{SOC} > I_{SOC} \\ \left(\frac{I_{SOC} - c_{SOC}}{I_{SOC}} \right)^2, c_{SOC} \leq I_{SOC} \end{cases} \tag{16}$$

and where $r_{pyr,a}$ is the pyrite oxidation rate for step (a) (mol·L^{-1}·day^{-1}); the term in curly brackets "{}" is the pyrite oxidation rate based on the equation from Prommer and Stuyfzand (2005), but with $k^*_{pyr,a}$ as the specific rate constant per unit concentration of microbes for step (a) (dm·mol·L^{-1}·day^{-1}); $c_{a,norm}$ is the normalized concentration of attached microbes (−); and I_{SOC} is the organic carbon inhibition constant (mol/L).

In order to reduce the number of calibrated parameters, p_2 and p_3 are fixed at the values given in Prommer and Stuyfzand (2005). Furthermore, $c_{H^+}^{-0.11}$ is regarded as constant as the impact on computed $c_{H^+}^{-0.11}$ values is minimal within the observed range of pH values (pH of 8.3 ± 0.1 results in $c_{H^+}^{-0.11} \approx 8.2 \pm 0.2$). Since our focus is on the main species (nitrate, nitrite, sulfate), this also eliminates the need to include other geochemical phenomena, which have an influence on the pH value, that is, calcite dissolution. These assumptions finally lead in combination with the normalized microbe concentrations to

$$r_{pyr,a} = \left\{ c_{NO_3^-}^{0.5} \cdot \left(K_{m,pyr,a} \cdot c_{pyr,0} \right) \cdot \left(\frac{c_{pyr}}{c_{pyr,0}} \right)^{2/3} \right\} \cdot c_{a,\mathrm{norm}} \cdot Z(c_{SOC}) \tag{17}$$

where $K_{m,pyr,a}$ ($= k^*_{pyr,a} \cdot p_4 \cdot c_{H^+}^{-0.11}$) is the specific rate constant for step (a) per initial concentration of pyrite and per unit concentration of microbes (day^{-1}).

For the second nitrite reduction (step (b)), the reaction is calculated with

$$r_{pyr,b} = \left\{ c_{NO_2^-}^{0.5} \cdot \left(K_{m,pyr,b} \cdot c_{pyr,0} \right) \cdot \left(\frac{c_{pyr}}{c_{pyr,0}} \right)^{2/3} \right\} \cdot c_{a,\mathrm{norm}} \cdot Z(c_{SOC}) \tag{18}$$

where $K_{m,pyr,b}$ is the specific rate constant for step (b) per initial concentration of pyrite and per normalized microbe concentration (day^{-1}).

Note that the pyrite rate law does not depend on the Fe^{2+} concentration and only applies to the irreversible reaction of pyrite dissolution under far from equilibrium conditions.

2.2.2.4. Reaction Network Implemented for Nitrate Reduction From Organic Carbon and Pyrite Oxidation Coupled With Microbial Transport Growth and Death

The final rate expressions implemented into HP1 for the major components: SOC, pyrite, nitrate, nitrite, sulfate, and attached and suspended microbes, are given in Table 1.

Table 1
Rate Expressions Used in HP1

Component	Rate Expressions
SOC	$r_{SOC} = r_{SOC,\,a} + r_{SOC,\,b}$
	$r_{SOC,a} = K_{m,SOC,a} \cdot c_{a,\mathrm{norm}} \cdot \frac{c_{SOC}}{c_{SOC}+k_{SOC,a}} \cdot \frac{c_{NO_3^-}}{c_{NO_3^-}+k_{NO_3^-}}$
	$r_{SOC,b} = K_{m,SOC,b} \cdot c_{a,\mathrm{norm}} \cdot \frac{c_{SOC}}{c_{SOC}+k_{SOC,b}} \cdot \frac{c_{NO_2^-}}{c_{NO_2^-}+k_{NO_2^-}}$
Pyrite	$r_{pyr} = r_{pyr,\,a} + r_{pyr,\,b}$
	$r_{pyr,a} = \left\{ c_{NO_3^-}^{0.5} \cdot \left(K_{m,pyr,a} \cdot c_{pyr,0}\right) \cdot \left(\frac{c_{pyr}}{c_{pyr,0}}\right)^{2/3} \right\} \cdot c_{a,\mathrm{norm}} \cdot Z(c_{SOC})$
	$r_{pyr,b} = \left\{ c_{NO_2^-}^{0.5} \cdot \left(K_{m,pyr,b} \cdot c_{pyr,0}\right) \cdot \left(\frac{c_{pyr}}{c_{pyr,0}}\right)^{2/3} \right\} \cdot c_{a,\mathrm{norm}} \cdot Z(c_{SOC})$
	$Z(c_{SOC}) = \begin{cases} 0 & , c_{SOC} > I_{SOC} \\ \left(\frac{I_{SOC} - c_{SOC}}{I_{SOC}}\right)^2 & , c_{SOC} \le I_{SOC} \end{cases}$
Normalized microbes, suspended	$r_{s,norm} = -k_{att} \cdot c_{s,norm} + k_{det} \cdot c_{a,norm} - d \cdot c_{s,norm}$
Normalized microbes, attached	$r_{a,norm} = k_{att} \cdot c_{s,norm} - k_{det} \cdot c_{a,norm} - d \cdot c_{a,norm} + (Y_{SOC} \cdot (r_{SOC,\,a} + r_{SOC,\,b}) + Y_{pyr} \cdot (r_{pyr,\,a} + r_{pyr,\,b}))$
Nitrate	$r_{NO_3^-} = 2 \cdot r_{SOC,a} + \frac{15}{2} \cdot r_{pyr,a}$
Nitrite	$r_{NO_2^-} = -2 \cdot r_{SOC,a} - \frac{15}{2} \cdot r_{pyr,a} + \frac{4}{3} \cdot r_{SOC,b} + 5 \cdot r_{pyr,b}$
Sulfate	$r_{SO_4^{2-}} = -2 \cdot r_{pyr,a} - 2 \cdot r_{pyr,b}$

Note. Positive rates = decreasing concentration, negative rates = increasing concentration.

2.2.3. Initial and Boundary Conditions

Saturated water flow was simulated using a constant flux boundary with a constant Darcy velocity of 2.31 cm/day. The model domain was set to be initially saturated. Transport was simulated with a concentration flux boundary at the bottom of the column to mimic the injection of the artificial groundwater, while a zero-concentration gradient boundary was defined at the top of the column. For the reactive transport model water was injected with a composition that equals the mean groundwater chemistry within the Hessian Ried and with a 3- to 4-fold increase of the nitrate concentration compared to the mean value of 20 to 30 mg/L (Table 2).

Table 2
Artificial Groundwater Composition Used in the Simulations as Initial (c_{init}) and Injected (c_{inj}) Pore Water Composition at the Inlet Boundary

Species	c_{inj} in mmol/L	c_{init} in mmol/L
NO_3^-	1.52 ± 0.08	0.00
NO_2^-	0.00 ± 0.02	0.00
SO_4^{2-}	0.55 ± 0.06	0.55
Br^-	0.12 ± 0.02	0.00
Cl^-	0.75 ± 0.08	0.72
HCO_3^-	0.27 ± 0.06	2.20
Na^+	0.93 ± 0.06	0.77
Mg^{2+}	0.65 ± 0.04	0.16
Ca^{2+}	0.78 ± 0.06	1.58

The initial pore water chemistry assumes that the aquifer is initially free of nitrate and nitrite. The initial concentration of SOC $c_{SOC,0}$ was used as a calibration parameter. The concentration was initially estimated using the stoichiometry of equations (6) and (7), and numerically solving the equation

$$c_{SOC,0} = \frac{Q}{V_w} \cdot \int_{t_n}^{t_m} \left(\frac{5}{4} \cdot \left(c_{NO_3^-,in} - c_{NO_3^-}(t)\right) - \frac{3}{4} \cdot c_{NO_2^-}(t) \right) dt \qquad (19)$$

where $c_{SOC,0}$ is the initial concentration of SOC defined relative to the fluid volume, Q is the water volume flux (L/day), V_w is the water volume of the column (L), $c_{NO3-/NO2-}$ (t) are the measured concentrations at the outflow for nitrate and nitrite at the time t, $c_{NO3-,in}$ is the inflowing concentration

of nitrate, t_n is the time when the initial nitrate breakthrough is roughly complete (14 days), and t_m is the time of the last measurement before autolithotrophic denitrification begins (60 days). Derivation of equation (19) is given in Text S1 in the supporting information.

According to the CRS measurement, the initial pyrite concentration was 2.34 mmol/kg, assuming that all sulfidic sulfur was bound in pyrite.

The initial concentration of microbes is difficult to determine at laboratory scale and even more difficult at field scale. Many authors (Lee et al., 2009; Rodríguez-Escales et al., 2016) assume a value based on the literature. The rate formulations expressed the attached microbe concentrations normalized to their initial concentration; consequently, the initial normalized concentration of attached microbes is 1. The injected water was free of microbes, but the initial pore water was assumed to be in equilibrium with suspended and attached microbes. Suspended microbes are given with

$$c_{s,\mathrm{norm},0}\cdot k_{att} = c_{a,\mathrm{norm},0}\cdot k_{det} \Rightarrow c_{s,\mathrm{norm},0} = \frac{k_{det}}{k_{att}}\cdot c_{a,\mathrm{norm},0} = \frac{k_{det}}{k_{att}}\cdot 1 \tag{20}$$

where $c_{a/s,norm,0}$ are the initial normalized concentrations of attached and suspended microbes.

2.2.4. Numerical Model Calibration

2.2.4.1. Calibration of Conservative and Reactive Transport Parameter

Automated calibration of the conservative and reactive transport model is conducted with PEST (Model-Independent Parameter Estimation and Uncertainty Analysis; Doherty, 2016) following a similar approach as discussed in Jacques et al. (2012), where UCODE was used. PEST minimizes discrepancies between model simulated outputs and the corresponding measurements by minimizing the weighted sum of squared differences between the respective values. In the optimization procedure the significance of the included data types as well as measurement errors of the collected data are considered by weighting the measurements with the inverse of their measurement uncertainty. The normalized weights are $w\left(NO_3^-\right) = 0.3,\ \ w\left(NO_2^-\right) = 0.3, w\left(SO_4^{2-}\right) = 0.4$.

First, conservative transport model parameters of the sediment, porosity n and the dispersivity coefficient α, are estimated based on the calibration of the measured bromide tracer breakthrough curve.

The reactive transport model is calibrated with measured concentrations of NO_3^-, NO_2^-, and SO_4^{2-} in the outflow of the column and along the column using all four ports. Therefore, a total number of 462 observation points (3 species with 74 time steps at the outflow and 20 time steps at the ports) were used in the inversion. The reactive transport model focuses on the aqueous species and solids relevant for denitrification (NO_3^-, NO_2^-, N_2, SO_4^{2-}, SOC, pyrite, denitrifying microbes) and has a total of 14 model parameters (Table S1 in the supporting information). A multiple calibration step approach was selected to calibrate nine parameters. Four parameters were fixed using values from previous publications, because they are highly insensitive (k_{NO3-}, k_{NO2-}) or correlated too strongly with other parameters (k_{att}, d). Parameters $k_{SOC,a}$ and $k_{SOC,b}$ were set by manual trial-and-error because their sensitivity was highly nonlinear (Table S1). Rate constants and the growth parameter for heterotrophic denitrification are taken from Rodríguez-Escales et al. (2016) and divided by their initial microbe concentration to account for the usage of normalized microbe concentrations. The normalized growth yield for autolithotrophic denitrification Y_{pyr} is initially assumed to be the same as the initial fit for the heterotrophic growth yield Y_{SOC}. The rate constants for autolithotrophic denitrification are taken from Appelo et al. (1998). In contrast to published rate constants for denitrification, which account for the total number of electrons ($5e^-$), we separated the rate constants for the two denitrification steps to account for the lower numbers of electrons transferred per denitrification step ($2e^-$ for step (a) and $3e^-$ for step (b)).

Nine parameters were estimated in the inversion. The experiment showed a two-phase denitrification with heterotrophic denitrification at the beginning and autolithotrophic denitrification at the end with only a small transition phase. Therefore, we first calibrated those parameters which are solely related to heterotrophic denitrification. This calibration used the data between day 0 and day 60 resulting in 37 measurements per species in the outflow and 9 at each port. Only five parameters are estimated in this first calibration step: the rate constants $K_{m,SOC,a/b}$, the heterotrophic normalized growth yield Y_{SOC}, the initial concentration of reactive organic carbon $c_{SOC,0}$, and the detachment coefficient k_{det}.

The second calibration phase uses the full data set and the calibration parameters related to autolithotrophic denitrification: the rate constants $K_{m,pyr,a/b}$, the autolithotrophic normalized growth yield Y_{pyr}, and the detachment coefficient k_{det}. The parameters from the first phase are restricted to their 99.7% confidence intervals to account for the short transition phase except for the detachment coefficient, which showed only a low sensitivity for the first calibration step. Additionally, Tikhonov regularization (Doherty, 2015) is employed by setting the initial values as preferred values. A preliminary calibration is done without considering parameter overfitting (large parameter changes without significant improvement of the calibration fit). The final calibration then stopped when the measurement objective function (the model to measurement misfit) was 5% higher than in the preliminary calibration, thus reaching an acceptable calibration fit without significant parameter overfitting, which usually occurs in the last 5–10% of a calibration (Doherty, 2016).

2.2.4.2. Parameter Sensitivity and Model Uncertainty

PEST calculates composite sensitivities for all observation points and parameters (Doherty, 2016). Observation sensitivities provide a measure of how sensitive an observation is to the parameters in the calibration process. The composite sensitivity of each parameter evaluates the impact (sensitivity) of parameters on the model response. All parameters are log-transformed during the calibration, which makes their sensitivities comparable (Doherty, 2015).

Parameter and observation uncertainty are calculated by the PEST utility programs with a linearity assumption for the model and an assumed normal distribution (Doherty, 2016). The parameters share information and also contribute uncertainty to each other. Assuming model linearity this can be calculated with (Doherty, 2015)

$$r_{j\rightarrow i} = \frac{\sigma^2_{j\rightarrow i}}{\sigma^2_i} \tag{21}$$

where $r_{j\rightarrow i}$ is the relative uncertainty contribution of parameter j to parameter i, $\sigma^2_{j\rightarrow i}$ is the uncertainty variance of parameter i for "freezing" of parameter j, and σ_i is the uncertainty variance of parameter i.

3. Results

The total simulation time is 164 days with an initial time step of 0.1 s and a maximum time step of 1 hr. The Peclet and Courant number equaled 1.65 and 1.40, respectively. Therefore, numerical dispersion did not occur. The advection-dispersion equation was solved with an implicit time weighting and Galerkin finite element space weighting scheme.

3.1. Hydraulic and Biogeochemical Properties of the Investigated Sediment

3.1.1. Biogeochemical Properties of the Investigated Sediments

The sediment samples consisted mainly of sandy to silty Quaternary eolian deposits with a partially high TIC content between 2 and 42 g/kg. The sulfide content (measured as CRS) increased with depth from values below or close the limit of quantification (18 mg S/kg) to 100 mg S/kg (max. 150 mg S/kg) at a depth of 30 m. Especially a silt layer at 25–26-m depth showed high CRS and very high TOC contents, indicating a layer with high denitrification potential.

SEM and BSE analyses of sediments showed different types of iron–sulfur compounds (Kludt et al., 2016). Fine-graded sediments in the silt layer at 25–26-m depth contained platy hexagonal grains with a high iron and sulfur BSE signal, which may indicate iron sulfide phases like pyrrhotite (e.g., Horng and Roberts (2006) often found in fine graded anoxic sediments (Kao et al., 2004), or iron sulfate phases like jarosite as possible weathering products of pyrite. At 35–36-m depth framboidal pyrite was observed. These spherical aggregates consist of pyrite microcrystals (0.1–1 μm) often found in modern anoxic sedimentary deposits (Wilkin et al., 1996). Some uncertainties still remain how framboidal pyrite is formed, but some researchers postulate that they are associated with mineralization of bacterial strains, organic particles/colloids, or may be formed by abiotic transformation processes (Rimstidt & Vaughan, 2003; Wilkin & Barnes, 1997). Our SEM-BSE analyses suggest that different iron sulfide phases are present in the sediments, which may exhibit different denitrification kinetics related to their structure and surface area (q.v. Bosch et al., 2011). Yet in the absence of exact knowledge about the ratios of the different iron sulfide phases they are lumped together into a single phase (pyrite).

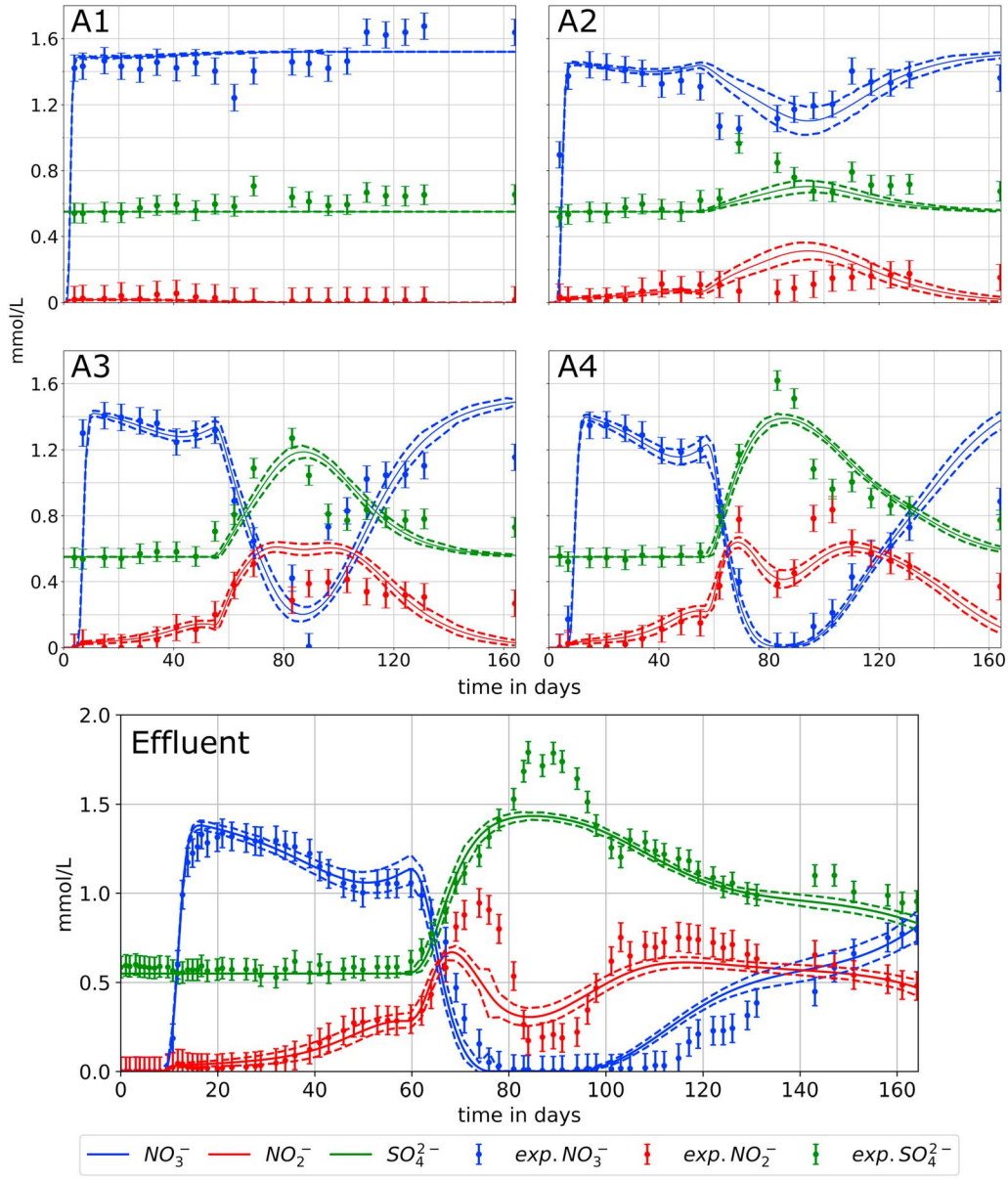

Figure 2. Transport model output (line) with 95% confidence interval (dashed line) and experimental data (points + error bars (95% confidence)) for the effluent and the sampling ports.

3.1.2. Conservative Transport Properties

The measured bromide breakthrough curve was used to calibrate dispersion and porosity with 3.03 mm and 0.54, respectively, as given in Figure S1 in the supporting information. The low dispersivity is likely due to the homogenization and careful packing of the sediment in the column (see section 2.1.2). The high porosity shows additionally that packaging was very loose.

3.2. Kinetic Processes for Nitrate Reduction in Pyritic Sediments

The experiments indicate two denitrification phases (Figure 2). The first phase lasted until day 60 and was dominated by heterotrophic denitrification. This is indicated by nitrate concentrations that remained below the concentration of nitrate in the injected water (difference of 0.2–0.5 mmol/L), while sulfate concentrations equaled the inflow concentration. Due to depletion of the bioavailable SOC the second phase initiated after day 60 and was dominated by autolithotrophic denitrification, as indicated by the strong decrease of nitrate

concentrations coupled with an increase of sulfate concentrations. Both denitrification phases showed a significant increase in nitrite concentration. However, for heterotrophic denitrification, nitrite increased only at later times, while for autolithotrophic denitrification it increased initially and dropped only when nitrate was nearly depleted. Although pyrite oxidation could be expected to lower the pH (see equations (12) and (13)), a constant pH was observed during the experiment (8.2–8.4) likely due to pH-buffering by calcite dissolution, as approximately 2.6 mol calcite per kg was present in the sediment material. Furthermore, ammonium concentrations were very low ($<$0.04 mmol/L) during the experiment, showing that denitrification was the major nitrate removal pathway. Additionally, very low iron(II/III) measurements ($<$0.003 mmol/L) during the entire experiment support the assumption of equation (12) that iron oxidation and precipitation occurred parallel to sulfide oxidation.

Measured sulfate concentrations are matched well in the discharge until day 80 and also between day 100 and day 160. The experimental data show a peak of the sulfate concentration between days 80 and 95. The simulated sulfate concentration strongly underestimates the measured sulfate peak. This difference is mainly caused by a different stoichiometry during this period than assumed in equations (12) and (13). There is up to 0.25 mmol/L sulfate more released than electron acceptors (nitrate and nitrite) were available for oxidation of pyrite. This means that besides pyrite other sulfur-containing minerals were dissolved by autolithotrophic denitrification and/or further sulfur sources exist like carbonate-associated sulfate, which could be released when calcite dissolves due to pH buffering. A further error can be related to the calculation of the pyrite surface area. The pyrite surface area is calculated in equations (17) and (18) with the assumption of an ideally dissolving cube/sphere. However, this assumption might not hold true for the experiment. The mismatch might also indicate the presence of different pyrite phases with different reactivity. A pyrite phase with a higher surface area per pyrite mass could be responsible for the initial sulfate peak around day 85, whereas a lower reactive phase with a lower surface area per pyrite mass that dissolved later might be responsible for the measured slower decline after day 120.

The simulated nitrate concentrations match the measured values well in the discharge until 100-day simulation time. However, nitrate concentrations are overestimated between day 100 and day 140, which might result from the fact that nitrite is slightly underestimated and sulfate concentrations are simulated well during this time period. The nitrite concentrations are replicated well for the heterotrophic phase, but show significant differences during the autolithotrophic denitrification peak, which is related to the mismatch for sulfate during that period.

Depth-dependent concentrations of nitrate, sulfate, and nitrite were measured at 10.75- (A1), 20.75- (A2), 30.75- (A3), and 40.75-cm (A4) depth along the column (Figure 2). Measured data at port A1 suggested that denitrification was limited in the first section of the column. The numerical model replicates this trend in general, but underestimates the denitrification rate at this shallow depth and thus also underestimates the small sulfate peak around day 70.

At 20.75-cm depth (A2), denitrification slightly increased, and thus, the nitrate minimum and sulfate maximum observed in the discharge also developed although 20 days earlier. Thus, at this depth, the model is in general able to replicate the observed trends for nitrate; however, the sulfate peak in the model is delayed by 20 days and is significantly underestimated, whereas nitrite is significantly overestimated. At 30.75- (A3) and 40.75-cm depth (A4), denitrification increased to rates as observed at the bottom of the column resulting in similar concentrations of nitrate, nitrite, and sulfate as measured in the discharge. The mismatch at ports A1 and A2 can be explained by the simulated high depletion of denitrifying microbes in the first section of the column (see section 3.3.1). The employed microbial transport approach is unable to produce sufficiently high microbe concentrations in the first section of the column, without increasing the microbe concentrations in the middle and last sections. Additionally, there is no other factor, which could be responsible for the underestimated denitrification rate especially for autolithotrophic denitrification in the first section of the column, as the sediment material was homogenized. Thus, no reactivity difference should exist between different sections of the column. Underestimation of autolithotrophic denitrification in the first section of the column leads to an overestimation of autolithotrophic denitrification and an earlier and intense pyrite depletion in the middle and last sections (ports A3 and A4). Finally, this results in an underestimation of the denitrification rate at the end of the simulation time (after day 160), resulting in an underestimation of nitrite and sulfate concentrations and overestimation of nitrate concentrations. The

Table 3
Calibrated Parameter Values, Confidence Limits, and Composite Parameter Sensitivities S for the Reactive Transport Model

Parameter	Calibrated Value	95% Confidence Interval Min	95% Confidence Interval Max	Literature	S
$K_{m,SOC,a}$ (mol L^{-1} day^{-1})	9.02×10^{-6}	7.73×10^{-6}	10.1×10^{-6}	1.52×10^{-2} [e], 5.58×10^{-4} [f], 8.73×10^{-5} [d], 7.51×10^{-4} [g], 2.36×10^{-4} [h]	1.33
$K_{m,SOC,b}$ (mol L^{-1} day^{-1})	3.04×10^{-5}	2.46×10^{-5}	3.75×10^{-5}	2.28×10^{-2} [e], 1.31×10^{-4} [d], 1.13×10^{-3} [f], 3.54×10^{-4} [h]	0.71
$c_{SOC,0}$ (mol/L)	1.75×10^{-3}	1.51×10^{-3}	2.02×10^{-3}	-	0.42
Y_{SOC} (L/mol)	1.19×10^{4}	0.99×10^{4}	1.43×10^{4}	3.06×10^{2} [e], 9.67×10^{2} [f], 4.29×10^{3} [d], 6.81×10^{3} [g], 2.97×10^{4} [h], 5.81×10^{4} [h]	1.88
Y_{pyr} (L/mol)	6.08×10^{3}	4.01×10^{3}	9.22×10^{3}	-	0.15
$K_{m,pyr,a}$ (day^{-1})	1.68×10^{-1}	1.10×10^{-1}	2.57×10^{-1}	0.21×10^{-1} [a*], 1.69×10^{-1} [b]	0.13
$K_{m,pyr,b}$ (day^{-1})	1.73×10^{-1}	1.13×10^{-1}	2.66×10^{-1}	0.31×10^{-1} [a*], 2.47×10^{-1} [b]	0.07
I_{SOC} (mol/L)	2.11×10^{-4}	1.13×10^{-4}	3.94×10^{-4}	-	0.05
k_{det} (day^{-1})	2.93×10^{0}	2.12×10^{0}	4.04×10^{0}	0.36×10^{0} to 2.16×10^{0} [c], 3.20×10^{-1} [d], 4.29×10^{-1} [d]	0.04

Note. The literature values for $K_{m,SOC,a/b}$, Y_{SOC}, and $K_{m,pyr,a/b}$ are calculated using their definitions in equations (4), (10), (11), (17), and (18) using the values from the respective studies.
[a]Prommer and Stuyfzand (2005). [b]Appelo et al. (1998). [c]Hornberger et al. (1992). [d]Clement et al. (1997). [e]Rodríguez-Escales et al. (2016). [f]Lee et al. (2009). [g]Lee et al. (2006). [h]Calderer et al. (2010).

denitrification decline at the end of the simulation results from the decrease of available pyrite for denitrification.

Also, microbial decay might influence the reduction of the denitrification rate at the end of the experiment. The microbial decay coefficient was not included in the model calibration. Test runs showed that variations of the microbial decay coefficient had a limited effect on the model fit.

Nitrite concentrations are overestimated in the first section of the column (ports A2 and A3) and partly underestimated in the last section (discharge and port A4). The experimental data shows a significant rate for nitrite reduction from the beginning of autolithotrophic denitrification (especially in port A2), but also a decrease of the nitrite reduction rate with distance and a rate increase when nitrate is nearly depleted. This mismatch between the measured and simulated concentrations is caused by a higher complexity for nitrite reduction during autolithotrophic denitrification than the model assumes, that is, a decrease of nitrite reduction with depth and an increase when nitrate is depleted.

The reactive transport model used a joint inversion of nitrate, nitrite, and sulfate concentrations at the outflow and at four locations along the column. The limited heterotrophic denitrification is simulated well at ports A2 to A4 and for the discharge, whereas the autolithotrophic denitrification was more difficult to replicate. A further assessment of the calibration using the root-mean-square error is given in the Text S2 and Table S2 in the supporting information. Possible factors that are responsible for these difficulties to simulate autolithotrophic denitrification are (i) missing measurements of denitrifying microbes, (ii) the overestimation of simulated nitrite concentration in the first section of the column, and (iii) an uncertainty about the sulfide mineral composition. The integration of an SOC inhibition for autolithotrophic denitrification enabled the model to mimic the temporal sequence of the two denitrification phases (heterotrophic followed by autolithotrophic denitrification). Also, coupling heterotrophic and later autolithotrophic denitrification with microbial growth and decay was found to be a suitable approach to simulate the measured data.

3.3. Kinetic Parameters for Nitrate Reduction in Pyritic Aquifers

3.3.1. Estimated Kinetic Parameter and Reaction Rates

The aim of our numerical investigations was to identify key parameters and processes that drive denitrification in pyritic aquifers. Based on the model calibration nine parameters were estimated for the reactive transport processes. The calibrated values lie in the range of values found by other researchers (Table 3). Furthermore, the confidence intervals for all parameters are relatively low due to the multiple-step calibration procedure. Additionally, the normalized growth yield for heterotrophic denitrification, Y_{SOC} with 1.2×10^4 L/mol, is about 2 times larger than for autolithotrophic denitrification with $Y_{pyr} = 0.61 \times 10^4$ L/mol (with respect to the transferred electrons this increases to 7.5), showing that microbial yield is higher for heterotrophic denitrification. This might also explain the preference for the highly reactive SOC compared to pyrite resulting in the temporal order of heterotrophic and autolithotrophic denitrification.

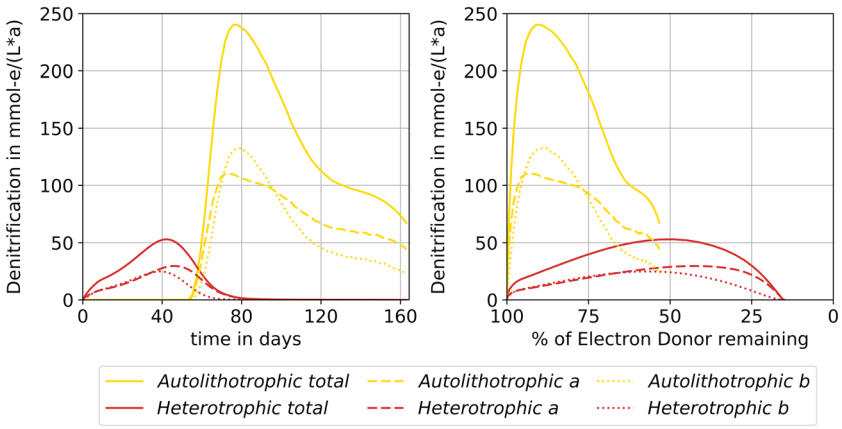

Figure 3. Model denitrification rates expressed with respect to mmol-e for nitrate and nitrite and autolithotrophic and heterotrophic denitrification, respectively. (left) As time series and (right) compared to the remaining electron donors.

The highest heterotrophic denitrification rate calculated over the 160-day simulation time was 53 mmol-e/(L*a) and was 4 times smaller than the highest autolithotrophic denitrification rate with 240 mmol-e/(L*a) (Figure 3). Furthermore, the denitrification rate for step (b) is similar to step (a) during heterotrophic denitrification, except for the end of the first phase. However, during autolithotrophic denitrification, the denitrification rate is larger for step (a) than for step (b) during most of the time. Only during the quick and complete consumption of nitrate between day 80 and 100 the denitrification rate is larger for step (b) than for step (a). Even though nitrite accumulates quite significantly in the model (up to 0.6 mmol/L), the model simulates that nitrite reduction always occurred and is solely caused by the different denitrification rates for both steps. The right part of Figure 3 shows that especially the autolithotrophic denitrification rate decreases strongly after only approximately 15% of the pyrite has been consumed.

The reactive transport model includes the calculation of normalized concentration profiles of microbes along the column (Figure 4). Five time steps were selected: initial heterotrophic denitrification (day 30), transition phase (day 60), autolithotrophic denitrification peak (day 90), denitrification decline (day 120), and the end of the model calculations (day 160). During heterotrophic denitrification microbes increase up to 2.5 times with respect to their initial concentration. At day 30, the highest concentrations occur in shallower parts of the column, when nitrate concentrations are highest. At day 60, this peak has moved to greater depths as SOC is mostly depleted. During the highest autolithotrophic denitrification (day 90), a new microbe concentration peak appears, rising 4 times above the initial concentration. This peak then moves downward when the pyrite concentration starts to fall. The model predicts that significant concentrations of SOC and pyrite still remain at shallow depths until the end of the experiment. However, for pyrite this remaining concentration is overestimated, indicated by the mismatch of sulfate at port A2. In the simulations a further decrease of

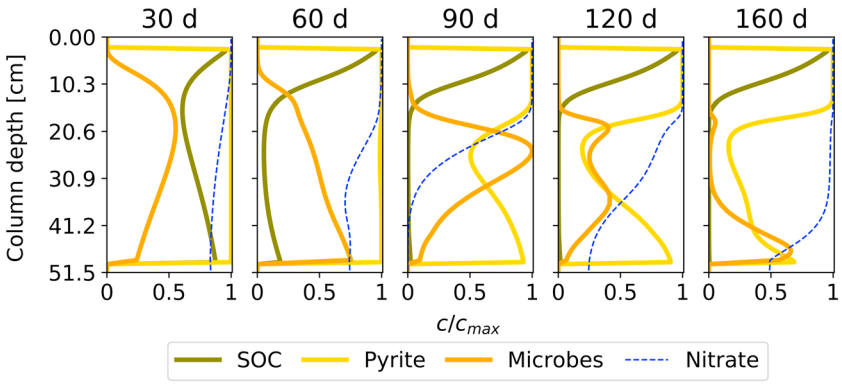

Figure 4. Microbial distribution and remaining electron donors normalized to their maximum value in the model column at five important time steps with nitrate as comparison.

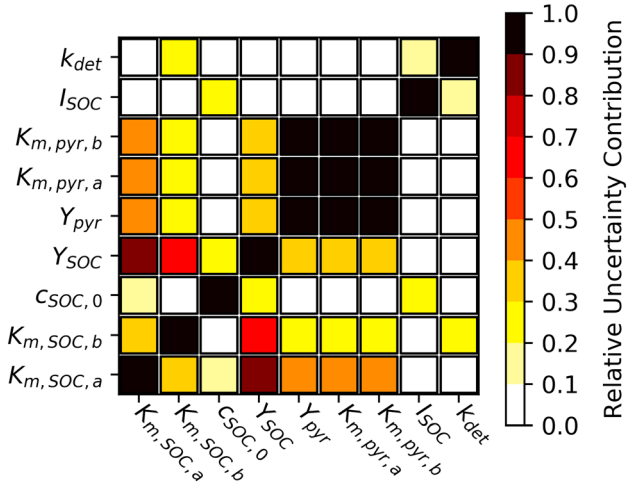

Figure 5. Relative uncertainty contribution between parameters around the calibrated best fit.

the denitrification at shallower depths is caused by the depletion of microbes due to the inflowing water free of microbes. Finally, after 160-day simulation time about 85% of the SOC (corresponds to 0.5% of the TOC) and 46% of the pyrite was depleted during the 5-month experiment and nitrate concentrations increase to 50 mg/L or 50% of the inflow concentration.

3.3.2. Sensitivity and Uncertainty of Kinetic Parameters

PEST was used to compute parameter sensitivities and uncertainties. Sensitivities for the log-transformed parameters varied between 0.04 and 1.9 (Table 3). Parameters used to simulate heterotrophic denitrification ($K_{m,SOC,a/b}$, $c_{SOC,0}$, Y_{SOC}) have the highest sensitivities even though rates for heterotrophic denitrification are lower than those for autolithotrophic denitrification. However, this results from the coupling and the temporal order of both processes: heterotrophic denitrification parameters affect the results of the first phase and also the beginning of autolithotrophic denitrification, while the parameters for autolithotrophic denitrification have no impact on the model behavior before day 60 as equations (17) and (18) include an exclusion for pyrite oxidation as long as the SOC concentration remains above the threshold value for I_{SOC}. Small changes of parameters for heterotrophic denitrification shift the start of autolithotrophic denitrification with strong gradients for nitrate and sulfate, creating large discrepancies between the model results and measurement concentration, resulting in high sensitivities. Small changes for parameters included in autolithotrophic denitrification change the slope of the nitrate decline and sulfate rise, respectively, around day 70. This results in a smaller mismatch between simulated and measured data, and smaller parameter sensitivities. Additionally, the observation sensitivities calculated by PEST also indicate that the time frame from day 60 to 80 was most important for the calibration (see Text S3 and Figure S2 in the supporting information).

Rate constants for the degradation of nitrite have a lower sensitivity for both processes, heterotrophic and autolithotrophic denitrification. This lower sensitivity results from missing measurements of nitrogen for the model calibration.

Parameters with the highest sensitivities have the lowest uncertainty if they do not correlate significantly with other parameters. Our calculation of the uncertainty shows that a significant correlation exists (Table 3). For example, the detachment coefficient, which is less sensitive compared to the other parameters, has a similar uncertainty as the more sensitive heterotrophic rate constants due to the fact that the heterotrophic rate constants correlate with other parameters.

Parameter correlation leads to the contribution of uncertainty between parameters. The relative uncertainty contribution between all parameters was calculated, displaying how much the uncertainty variance of each parameter will drop if another is held constant and the model would behave perfectly linearly. The uncertainty matrix (Figure 5) shows that uncertainty contribution is quite high for some parameter combinations, especially between the normalized growth yields and rate constants. Most parameters are difficult to measure or to obtain from lab experiments or even more difficult at field scale. For example, $c_{SOC,0}$ might be known for laboratory experiments. However, measured TOC might overestimate the more relevant kinetic parameter, reactive SOC. The normalized growth yields $Y_{SOC/pyr}$ (in this study defined as growth yield $y_{soc/pyr}$ divided by the initial microbe concentration) can be obtained if the initial microbe concentration is measured. If the growth yield of a specific microbial species is also known these measurements would significantly decrease the uncertainty of the rate constants.

3.4. Isotopic Fingerprint During Nitrate Reduction

In the sediments, a mean δ^{34}S-sulfide (CRS) value of −15.5‰ (n = 11, σ = 2.9) was measured (Kludt et al., 2016). Since there is no isotopic fractionation of solid sulfide during oxidation processes (Knöller et al., 2005; Seal, 2006; Vaughan, 2006), this can be assumed as a constant input value for δ^{34}S into the water phase during the autolithotrophic denitrification.

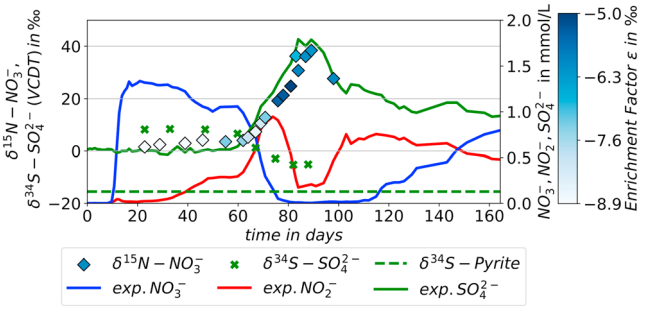

Figure 6. Measured isotopic sulfate and nitrate isotopic signatures with the enrichment factor ε (15 N-nitrate).

At the beginning of the experiment, a $\delta^{34}S$ value of the dissolved sulfate of about 8.2‰ was measured. With increasing sulfate concentrations, the $\delta^{34}S$-SO_4^{2-} values decreased and reached a minimum of −5.2‰. Thus, the dissolved sulfate approached the $\delta^{34}S$ value of the sedimentary sulfide (Figure 6). This suggests in accordance with the model results that the increase in sulfate concentration originated from oxidation of sulfides in the sediment (autolithotrophic denitrification). The proportion of sulfide oxidation during autolithotrophic denitrification can be estimated based on the sulfate concentration and isotope values on day 87 of the experiment. The initial sulfate concentration was 0.6 mmol/L with a $\delta^{34}S$ value of 8.2‰. Therefore, 1.1 mmol/L sulfate with a $\delta^{34}S$ value of −12.5‰ were necessary to obtain a measured sulfate concentration of 1.7 mmol/L with $\delta^{34}S$ of −5.2‰ at day 87.

In contrast to the sulfur isotopes, nitrate isotopes ($\delta^{15}N$-NO_3^-) show fractionation during the denitrification process. At the beginning of the column experiment the $\delta^{15}N$-NO_3^- values were 0.5–2.5‰ and increased during the experiment up to 38.4‰. The enrichment factors for denitrification (calculated as ε using the Rayleigh equation according to Knöller et al. (2011) and Mariotti et al. (1981); see also Text S4 in the supporting information) showed a range from −8.9 to −3.9‰ similar to other studies (Lehmann et al., 2003). The work of Frey et al. (2014) indicates that there is a measurable difference in the fractionation factors between autolithotrophic and heterotrophic denitrification. In addition, the fractionation factor of heterotrophic denitrification depends on the type of organic carbon and on the bacterial communities. During the column experiment, the phase with low (heterotrophic) nitrate degradation (up to day 75) showed enrichment factors between −8.9 and −7.3‰, whereas the phase with high (autolithotrophic) denitrification (after day 75) showed increased enrichment factors between −6.9 and −5.0‰ (Figure 6). These differences in the enrichment factors indicate a change in the denitrification processes.

Our isotopic measurements support the results of the reactive transport model showing that the sulfate increase occurring after day 60 originated mainly from a new source, pyrite oxidation, which started relatively abruptly. Therefore, the simulation of autolithotrophic denitrification was modeled with a zero rate for pyrite oxidation in the presence of higher SOC concentrations in equations (17) and (18) to achieve this behavior.

Similarly, the enrichment factor for ^{15}N shows that there was a process change between day 50 and day 80, from heterotrophic to autolithotrophic denitrification. Thus, both isotopic analysis and model results demonstrate that significant heterotrophic denitrification ended around day 60 and the sulfate increase was the consequence of pyrite oxidation during autolithotrophic denitrification and did not result from dissolution of other minerals like gypsum. The enrichment factor in Figure 6 also indicates, that nitrite accumulation or the conditions that lead to it (SOC close to depletion), increase the enrichment factor during heterotrophic denitrification. During autolithotrophic denitrification the accumulation of nitrite apparently lead to lower enrichment factor values as a significant increase can be observed after the nitrite spike around day 70.

4. Discussion

4.1. Comparison With Existing Literature Values

The observed denitrification rates reached values up to 11 mmol-N/(L*a) for heterotrophic denitrification and up to 48 mmol-N/(L*a) for autolithotrophic denitrification and are close to those described by Carrey et al. (2013) for column experiments with sediments that contain organic carbon and pyrite (e.g., 9.5–36.8 mmol-N/(L*a)). However, they showed using $\delta^{34}S$ that autolithotrophic denitrification was insignificant even though the sediment was described as pyrite rich. The column experiment of Carrey et al. (2013) ran over 12 months where at the end the denitrification potential appears to be depleted without autolithotrophic denitrification occurring; therefore, an inhibition of autolithotrophic denitrification as in our experiment has not occurred. The difference is possibly due to different microbe species in the sediments or due to the sulfide minerals being coated and therefore unavailable for reaction. Jorgensen et al. (2009)

reported 3.6–5.8 mmol-N/(L*a) in incubation experiments also with sulfides and organic carbon. The experiments from Jorgensen et al. (2009) were conducted with similar electron donor concentration compared to our sediment but using a low temperature of 9 °C compared to our experiments at room temperature (20 °C), which can explain the lower denitrification rates. For sediments with similar electron donor concentrations denitrification rates determined at field scale are often lower (e.g., 0.016 (Böhlke et al., 2002), 0.97 mmol-N/(L*a) (Korom et al., 2012)). This might be caused by a lower reactivity of the electron donors as, for example, in Korom et al. (2012), other minerals than pyrite were consumed during denitrification.

4.2. Impact of Porosity

The high porosity value obtained from the tracer experiment indicated a very loose packing of the sediment. After the experiment was finished and the column was opened, compaction of 5 cm (≈10% of the column) was observed. This compaction might have occurred during the initial saturation or slowly over time. This would suggest that the pore water velocity inside the sediment increased, since porosity decreased, which should result in less denitrification and higher nitrate concentrations at the outflow, since there is less time for denitrification. If porosity decreases from 0.54 to 0.44, the pore water velocity will increase by about 22% and the mean travel time through the sediment in the column will decrease by about 26%. However, the impact on the model response was only small indicated by the obtained calibration fit. An alternative model geometry, which assumes that compaction occurred during saturation, was also tested but yielded a slightly worse model calibration fit than the model presented here.

4.3. SOC-DOC Transformation

Previous studies have shown that SOC is typically first transformed to more reactive DOC, which is then oxidized (Komada et al., 2012; Weston & Joye, 2005). In our model SOC oxidizes directly; this simplification assumes that SOC-DOC transformation is immediately followed by DOC oxidation, meaning free DOC does not occur in significant concentrations. The model fits the data reasonably well for the heterotrophic phase, indicating that this assumption holds true for our experiment. To avoid adding further processes without having measurements the SOC-DOC transformation was neglected. This simplification limits the model for systems where DOC oxidation is slower or inflow of DOC is significant. However, the DOC oxidation kinetics can be added similar to the SOC kinetics with an additional term for the transformation kinetics as given in Wriedt and Rode (2006).

4.4. Electron Donor Limitation

The amount of TOC available for denitrification was very low, only about 0.5%, which can be regarded as typical for sediments, which are not in a zone with a high influx of DOC-rich water like riparian or hyporheic zones (Rivett et al., 2008). After the modeled time frame about 46% of the pyrite has been oxidized, but nitrate concentrations are again reaching high concentrations with the denitrification rate going further down. It is possible that the remaining pyrite surfaces are getting coated by iron hydroxides, which are insoluble at the occurring pH of 8.2 ± 0.1. This could also explain some of the model misfits at the end of modeled time frame when such a coating can be expected to be highest.

4.5. Natural Heterogeneity

In natural aquifer systems denitrification is often affected by heterogeneity due to different distributions of hydraulic parameters or electron donor concentrations (e.g., Arora & Mohanty, 2017; Dwivedi et al., 2018). An experimental setup with a homogenized sediment sample from one single layer of a borehole cannot reflect these effects. However, our results can improve our understanding of processes in the (quasi-)homogeneous layers/zones, which can then be transferred into a 2-D/3-D model of heterogeneous systems. This step-by-step approach is relevant as in natural heterogeneous systems; it is often difficult to separate between the effects of the not well-known heterogeneity or another kinetic process.

4.6. Microbial Growth

The growth of microorganisms in porous media can influence the hydraulic properties of the subsurface through clogging of the pore space (e.g., Taylor & Jaffé, 1990). The effects can be expected to be strongest when microbial concentrations are the highest, in our case around day 90 (see Figures 2 and 4). However, the misfit between the measured and simulated sulfate concentration at this time cannot be explained by

changes in hydraulic conductivity or porosity. In general, since the porosity of our sediment is high it is very likely that the microbial growth has no significant effect on the hydraulic properties of the sediment.

4.7. Further Sources of Organic Carbon

A source for organic carbon for heterotrophic denitrification that is not included in the model is the carbon of the microbes, also called endogenous respiration. Rodríguez-Escales et al. (2014) have shown that the importance of endogenous respiration can vary relative to exogenous respiration with ethanol and glucose but found that for the overall denitrification fluxes endogenous respiration was insignificant. Since we obtained no samples/measurements for total microbial or biomass concentration, the initial concentration can only be assumed and we introduced a normalized concentration to avoid such an assumption. Since the assumed value for the initial concentration would affect how much carbon would be stored in the microbial biomass, the importance of endogenous respiration cannot be clearly shown with our data.

4.8. Nitrite Accumulation

Nitrite accumulates in our experiment for both heterotrophic and autolithotrophic denitrification, a phenomenon, which has been observed in a multitude of studies (e.g., Bosch et al., 2011; Carrey et al., 2013; Mastrocicco et al., 2011; Parmentier et al., 2014). It was observed that the rates for nitrate and nitrite reduction are affected differently by specific environmental conditions. Mastrocicco et al. (2011) observed in batch experiments that nitrite reduction may be inhibited by the presence of nitrate when electron donors are limited due to a competitive advantage of nitrate. The same was observed in our experiment for heterotrophic denitrification, where nitrite accumulated only when the bioavailable SOC was near depletion. For autolithotrophic denitrification, we observed that significant nitrite accumulation occurred. Other studies (e.g., Jorgensen et al., 2009) did not observe nitrite accumulation during autolithotrophic denitrification. The difference might be due to differences in temperature, pH, or microbiological species (Rivett et al., 2008; Vaclavkova et al., 2015). In Carrey et al. (2013) nitrate concentrations were always higher than nitrite concentrations with the exception of a short phase at the start of the experiment. In our experiments, nitrite was never completely reduced after its accumulation began in contrast to nitrate. Our results show that nitrite concentrations during autolithotrophic denitrification increased before nitrate concentrations increased again. This shows that a nitrite breakthrough could precede a nitrate breakthrough at a drinking water well downstream of a nitrate source. In drinking water, nitrite is more detrimental to human health than nitrate, and thus, we recommend that water samples are always analyzed for nitrite as well.

4.9. Isotopes

Our results show that the measurements of N isotopes can help to identify changes in the denitrification pathway, for example, from heterotrophic to autolithotrophic denitrification, especially if sulfate cannot be used as an indicator. Future investigations should include detailed measurements of N isotopes so that an improved reactive transport model can be developed that simulates the isotopic fractionation. This could also give further insight on how isotopic fractionation is influenced by nitrite accumulation.

5. Conclusions

Our results show that denitrification rates drop significantly before all electron donors are oxidized. For organic carbon, only a fraction is bioavailable, depending on the geologic history and the inflow of DOC. For pyrite, this is possibly caused by coating with insoluble iron(III)-hydroxides, but under different hydrochemical conditions, this might not occur. For the assessment of the denitrification potential of a sediment or an aquifer, TOC for heterotrophic denitrification and CRS for autolithotrophic denitrification might be used, but the geologic history of the sediment, the hydrochemistry, and the microbiology will have a significant influence on the amount, distribution, and availability of the electron donors for denitrification.

A temporal order of first heterotrophic followed by autolithotrophic denitrification was observed under steady state conditions, even though the maximum rates for autolithotrophic were higher. The preference of the denitrifying microbes for organic carbon assumed in the model should be studied in future experiments by an additional analysis of the microbial community (as, e.g., in Torrentó et al. 2011).

While our work investigates constant boundary conditions, natural systems are often highly transient and, for example, the inflow of oxygen in a predominantly anoxic region, or a change of pH or temperature, might

have profound influence on the denitrification potential, e.g., by remobilizing the coating around pyrite. Both transient hydraulic and also transient geochemical conditions on the denitrification processes should be investigated in further research.

The local sensitivity analysis has shown that in systems where a process precedes another, in our case heterotrophic before autolithotrophic denitrification, the parameter sensitivities of the first process can be significantly higher than expected. Furthermore, significant uncertainty contribution between parameters has been found. Although we can theorize that additional measurements, for example, for the biomass concentration, can reduce this effect.

Acknowledgments
Thanks are given to the Deutsche Bundesstiftung Umwelt (DBU), Germany, for a scholarship and to the Hessian Ministry for the Environment, Climate Protection, Agriculture and Consumer Protection for funding the laboratory experiments. We also would like to thank Frank-Andreas Weber and Christoph Schüth for supporting the laboratory work to conduct the column experiments, Kai Knöller for measuring the nitrate and sulfate isotopes, and three anonymous reviewers for their comments and suggestions. The data used are shown in the figures or listed in the tables and supporting information.

References

André, L., Pauwels, H., Dictor, M. C., Parmentier, M., & Azaroual, M. (2011). Experiments and numerical modelling of microbially-catalysed denitrification reactions. *Chemical Geology*, *287*(3–4), 171–181. https://doi.org/10.1016/j.chemgeo.2011.06.008

Antoniou, E. A., Stuyfzand, P. J., & van Breukelen, B. M. (2013). Reactive transport modeling of an aquifer storage and recovery (ASR) pilot to assess long-term water quality improvements and potential solutions. *Applied Geochemistry*, *35*, 173–186. https://doi.org/10.1016/j.apgeochem.2013.04.009

Appelo, C. A. J., Verweij, E., & Schäfer, H. (1998). A hydrogeochemical transport model for an oxidation experiment with pyrite/calcite/exchangers/organic matter containing sand. *Applied Geochemistry*, *13*(2), 257–268. https://doi.org/10.1016/S0883-2927(97)00070-X

Aravena, R., & Robertson, W. D. (1998). Use of multiple isotope tracers to evaluate denitrification in ground water: Study of nitrate from a large-flux septic system plume. *Ground Water*, *36*(6), 975–982. https://doi.org/10.1111/j.1745-6584.1998.tb02104.x

Arora, B., & Mohanty, B. P. (2017). Influence of spatial heterogeneity and hydrological perturbations on redox dynamics: A column study. *Procedia Earth and Planetary Science*, *17*, 869–872. https://doi.org/10.1016/j.proeps.2017.01.046

Arora, B., Spycher, N. F., Steefel, C. I., Molins, S., Bill, M., Conrad, M. E., et al. (2016). Influence of hydrological, biogeochemical and temperature transients on subsurface carbon fluxes in a flood plain environment. *Biogeochemistry*, *127*(2-3), 367–396. https://doi.org/10.1007/s10533-016-0186-8

Bergmann, A., van Straaten, L., van Berk, W., Dietrich, P., Franko, U., & Kiefer, J. (2013). Konsequenzen nachlassenden Nitratabbauvermögens in Grundwasserleitern, *Abschlussbericht im DVGW F&E-Vorhaben W1/06/08, Bearbeiter: C. Hansen, S. Wilde, F.-A. Weber, S. Häußler* (DVGW Deutscher Verein des Gas- und Wasserfaches e. V.).

BMUB, and BMEL (2016). Nitratbericht 2016 Gemeinsamer Bericht der Bundesministerien für Umwelt, Naturschutz, Bau und Reaktorsicherheit sowie für Ernährung und Landwirtschaft 141 pp., Bundesministerium für Umwelt, Naturschutz, Bau und Reaktorsicherheit (BMUB) & Bundesministerium für Ernährung und Landwirtschaft (BMEL)

Böhlke, J. K. (2002). Groundwater recharge and agricultural contamination. *Hydrogeology Journal*, *10*(1), 153–179. https://doi.org/10.1007/s10040-001-0183-3

Böhlke, J. K., Wanty, R., Tuttle, M., Delin, G., & Landon, M. (2002). Denitrification in the recharge area and discharge area of a transient agricultural nitrate plume in a glacial outwash sand aquifer, Minnesota. *Water Resources Research*, *38*(7), W1105. https://doi.org/10.1029/2001WR000663

Bosch, J., Lee, K.-Y., Jordan, G., Kim, K.-W., & Meckenstock, R. U. (2011). Anaerobic, nitrate-dependent oxidation of pyrite nanoparticles by *Thiobacillus denitrificans*. *Environmental Science & Technology*, *46*(4), 2095–2101. https://doi.org/10.1021/es2022329

Böttcher, J., & Strebel, O. (1987). Die mittlere Nitratkonzentration des Grundwassers in Sandgebieten in Abhängigkeit von der Bodennutzungsverteilung. *Wasser und Boden*, *8*, 383–387.

Bradley, P. M., Fernandez, M., & Chapelle, F. H. (1992). Carbon limitation of denitrification rates in an anaerobic groundwater system. *Environmental Science & Technology*, *26*(12), 2377–2381. https://doi.org/10.1021/es00036a007

Bragan, R. J., Starr, J. L., & Parkin, T. B. (1997). Shallow groundwater denitrification rate measurement by acetylene block. *Journal of Environmental Quality*, *26*(6), 1531–1538. https://doi.org/10.2134/jeq1997.00472425002600060012x

Calderer, M., Jubany, I., Pérez, R., Martí, V., & de Pablo, J. (2010). Modelling enhanced groundwater denitrification in batch microcosm tests. *Chemical Engineering Journal*, *165*(1), 2–9. https://doi.org/10.1016/j.cej.2010.08.042

Canfield, D. E., Raiswell, R., Westrich, J. T., Reaves, C. M., & Berner, R. A. (1986). The use of chromium reduction in the analysis of reduced inorganic sulfur in sediments and shales. *Chemical Geology*, *54*(1–2), 149–155. https://doi.org/10.1016/0009-2541(86)90078-1

Carrey, R., Otero, N., Soler, A., Gómez-Alday, J. J., & Ayora, C. (2013). The role of lower cretaceous sediments in groundwater nitrate attenuation in central Spain: Column experiments. *Applied Geochemistry*, *32*, 142–152. https://doi.org/10.1016/j.apgeochem.2012.10.009

Casciotti, K. L., Sigman, D. M., Hastings, M. G., Böhlke, J. K., & Hilkert, A. (2002). Measurement of the oxygen isotopic composition of nitrate in seawater and freshwater using the denitrifier method. *Analytical Chemistry*, *74*(19), 4905–4912. https://doi.org/10.1021/ac020113w

Clement, T. P., Peyton, B. M., Skeen, R. S., Jennings, D. A., & Petersen, J. N. (1997). Microbial growth and transport in porous media under denitrification conditions: Experiments and simulations. *Journal of Contaminant Hydrology*, *24*(3-4), 269–285. https://doi.org/10.1016/S0169-7722(96)00014-9

DIN19528 (2009). Elution von Feststoffen - Perkolationsverfahren zur gemeinsamen Untersuchung des Elutionsverhaltens von anorganischen und organischen Stoffen, edited, Deutsches Institut für Normung e. V.

DIN51724–2 (1999). Testing of solid fuels—Determination of sulfur content, edited, Deutsches Institut für Normung e. V.

Doherty, J. (2015). *Calibration and Uncertainty Analysis for Complex Environmental Models* (p. 237). Brisbane, Australia: Watermark Numerical Computing.

Doherty, J. (2016). *PEST: Model-Independent Parameter Estimation User Manual Part I: PEST, SENSAN and Global Optimisers* (p. 390). Brisbane, Australia: Watermark Numerical Computing.

Dwivedi, D., Arora, B., Steefel, C. I., Dafflon, B., & Versteeg, R. (2018). Hot spots and hot moments of nitrogen in a riparian corridor. *Water Resources Research*, *54*, 205–222. https://doi.org/10.1002/2017WR022346

Eckert, P., & Appelo, C. A. J. (2002). Hydrogeochemical modeling of enhanced benzene, toluene, ethylbenzene, xylene (BTEX) remediation with nitrate. *Water Resources Research*, *38*(8), 1130. https://doi.org/10.1029/2001WR000692

Engelhardt, I., Prommer, H., Schulz, M., Vanderborght, J., Schüth, C., & Ternes, T. A. (2014). Reactive transport of lomeprol during stream-groundwater interactions. *Environmental Science & Technology*, *48*(1), 199–207. https://doi.org/10.1021/es403194r

Ernstsen, V. (1996). Reduction of nitrate by Fe^{2+} in clay minerals. *The Clay Minerals Society*, *44*(5), 559–608.
Fossing, H., & Jørgensen, B. B. (1989). Measurement of bacterial sulfate reduction in sediments: Evaluation of a single-step chromium reduction method. *Biogeochemistry*, *8*(3), 205–222. https://doi.org/10.1007/bf00002889
Frey, C., Hietanen, S., Jürgens, K., Labrenz, M., & Voss, M. (2014). N and O isotope fractionation in nitrate during chemolithoautotrophic denitrification by *Sulfurimonas gotlandica*. *Environmental Science & Technology*, *48*(22), 13,229–13,237. https://doi.org/10.1021/es503456g
Ginn, T. R., Wood, B. D., Nelson, K. E., Scheibe, T. D., Murphy, E. M., & Clement, T. P. (2002). Processes in microbial transport in the natural subsurface. *Advances in Water Resources*, *25*(8–12), 1017–1042. https://doi.org/10.1016/S0309-1708(02)00046-5
Groffman, P. M., Davidson, E. A., & Seitzinger, S. (2009). New approaches to modeling denitrification. *Biogeochemistry*, *93*(1–2), 1–5. https://doi.org/10.1007/s10533-009-9285-0
Hansen, C., Bergmann, A., Weber, F.-A., van Straaten, L., Wilde, S., Häußler, S., et al. (2011). Konsequenzen nachlassenden Nitratabbaus in Grundwasserleitern, *ewp - energie wasser*. *Praxis*, *10*, 44–49.
Hansen, H. C. B., & Koch, C. B. (1998). Reduction of nitrate to ammonium by sulphate green rust: Activation energy and reaction mechanism. *Clay Minerals*, *33*(01), 87–101. https://doi.org/10.1180/000985598545453
Hiscock, K. M., Lloyd, J. W., & Lerner, D. N. (1991). Review of natural and artificial denitrification of groundwater. *Water Research*, *25*, 1099–1111. https://doi.org/10.1016/0043-1354(91)90203-3
Hofstetter, T. B., Schwarzenbach, R. P., & Haderlein, S. B. (2002). Reactivity of Fe (II) species associated with clay minerals. *Environmental Science & Technology*, *37*(3), 519–528. https://doi.org/10.1021/es025955r
Hornberger, G. M., Mills, A. L., & Herman, J. S. (1992). Bacterial transport in porous media: Evaluation of a model using laboratory observations. *Water Resources Research*, *28*, 915–923. https://doi.org/10.1029/91WR02980
Horng, C.-S., & Roberts, A. P. (2006). Authigenic or detrital origin of pyrrhotite in sediments?: Resolving a paleomagnetic conundrum. *Earth and Planetary Science Letters*, *241*(3–4), 750–762. https://doi.org/10.1016/j.epsl.2005.11.008
Jacques, D., Šimůnek, J., Mallants, D., & Genuchten, M. T. v. (2018). The HPx software for multicomponent reactive transport during variably-saturated flow: Recent developments and applications. *Journal of Hydrology and Hydromechanics*, *66*(2), 211–226. https://doi.org/10.1515/johh-2017-0049
Jacques, D., Smith, C., Šimůnek, J., & Smiles, D. (2012). Inverse optimization of hydraulic, solute transport, and cation exchange parameters using HP1 and UCODE to simulate cation exchange. *Journal of Contaminant Hydrology*, *142-143*, 109–125. https://doi.org/10.1016/j.jconhyd.2012.03.008
Jorgensen, C. J., Jacobsen, O. S., Elberling, B., & Aamand, J. (2009). Microbial oxidation of pyrite coupled to nitrate reduction in anoxic groundwater sediment. *Environmental Science & Technology*, *43*(13), 4851–4857. https://doi.org/10.1021/es803417s
Kao, S.-J., Horng, C.-S., Roberts, A. P., & Liu, K.-K. (2004). Carbon–sulfur–iron relationships in sedimentary rocks from southwestern Taiwan: Influence of geochemical environment on greigite and pyrrhotite formation. *Chemical Geology*, *203*(1–2), 153–168. https://doi.org/10.1016/j.chemgeo.2003.09.007
Kludt, C., Weber, F.-A., Bergmann, A., Knöller, K., Berthold, G., & Schüth, C. (2016). Identification of denitrification processes and prognoses of denitrification potential in the sediments of the hessian Ried. *Grundwasser*, *21*(3), 227–241. https://doi.org/10.1007/s00767-015-0317-5
Knöller, K., Trettin, R., & Strauch, G. (2005). Sulphur cycling in the drinking water catchment area of Torgau-Mockritz (Germany): Insights from hydrochemical and stable isotope investigations. *Hydrological Processes*, *19*(17), 3445–3465. https://doi.org/10.1002/hyp.5980
Knöller, K., Vogt, C., Haupt, M., Feisthauer, S., & Richnow, H.-H. (2011). Experimental investigation of nitrogen and oxygen isotope fractionation in nitrate and nitrite during denitrification. *Biogeochemistry*, *103*(1–3), 371–384. https://doi.org/10.1007/s10533-010-9483-9
Kölle, W. (1984). Auswirkungen von Nitrat in einem reduzierenden Grundwasserleiter. *DVGW-Schriftenreihe Wasser*, *38*, 156–167.
Kölle, W., Werner, P., Strebel, O., & Böttcher, J. (1983). Denitrifikation in einem reduzierenden Grundwasserleiter. *Vom Wasser*, 125–147.
Komada, T., Polly, J. A., & Johnson, L. (2012). Transformations of carbon in anoxic marine sediments: Implications from $\Delta^{14}C$ and $\delta^{13}C$ signatures. *Limnology and Oceanography*, *57*(2), 567–581. https://doi.org/10.4319/lo.2012.57.2.0567
Konrad, C. (2006). Methoden zur Bestimmung des Umsatzes von Stickstoff, dargestellt für drei pleistozäne Grundwasserleiter Norddeutschlands, TU Dresden.
Korom, S. F., Schuh, W. M., Tesfay, T., & Spencer, E. J. (2012). Aquifer denitrification and in situ mesocosms: Modeling electron donor contributions and measuring rates. *Journal of Hydrology*, *432-433*, 112–126. https://doi.org/10.1016/j.jhydrol.2012.02.023
Lee, E. J., Kim, M., Kim, Y., & Lee, K.-K. (2009). Numerical and field investigation of enhanced in situ denitrification in a shallow-zone well-to-well recirculation system. *Ecological Modelling*, *220*(19), 2441–2449. https://doi.org/10.1016/j.ecolmodel.2009.06.014
Lee, M.-S., Lee, K.-K., Hyun, Y., Clement, T. P., & Hamilton, D. (2006). Nitrogen transformation and transport modeling in groundwater aquifers. *Ecological Modelling*, *192*(1–2), 143–159. https://doi.org/10.1016/j.ecolmodel.2005.07.013
Lehmann, M. F., Reichert, P., Bernasconi, S. M., Barbieri, A., & McKenzie, J. A. (2003). Modelling nitrogen and oxygen isotope fractionation during denitrification in a lacustrine redox-transition zone. *Geochimica et Cosmochimica Acta*, *67*(14), 2529–2542. https://doi.org/10.1016/S0016-7037(03)00085-1
Liao, L., Green, C. T., Bekins, B. A., & Böhlke, J. K. (2012). Factors controlling nitrate fluxes in groundwater in agricultural areas. *Water Resources Research*, *48*, W00L09. https://doi.org/10.1029/2011WR011008
Maggi, F., Gu, C., Riley, W. J., Hornberger, G. M., Venterea, R. T., Xu, T., et al. (2008). A mechanistic treatment of the dominant soil nitrogen cycling processes: Model development, testing, and application. *Journal of Geophysical Research*, *113*, G02016. https://doi.org/10.1029/2007JG000578
Mariotti, A., Germon, J. C., Hubert, P., Kaiser, P., Letolle, R., Tardieux, A., & Tardieux, P. (1981). Experimental determination of nitrogen kinetic isotope fractionation: Some principles; illustration for the denitrification and nitrification processes. *Plant and Soil*, *62*(3), 413–430. https://doi.org/10.1007/bf02374138
Mastrocicco, M., Colombani, N., Salemi, E., & Castaldelli, G. (2011). Reactive modeling of denitrification in soils with natural and depleted organic matter. *Water, Air, & Soil Pollution*, *222*(1-4), 205–215. https://doi.org/10.1007/s11270-011-0817-6
Molins, S., Greskowiak, J., Wanner, C., & Mayer, K. U. (2015). A benchmark for microbially mediated chromium reduction under denitrifying conditions in a biostimulation column experiment. *Computational Geosciences*, *19*(3), 479–496. https://doi.org/10.1007/s10596-014-9432-0
Parkhurst, D. L., & Appelo, C. A. J. (2013). Description of input and examples for PHREEQC version 3—A computer program for speciation, *Batch-Reaction, One-Dimensional Transport, and Inverse Geochemical Calculations,* 497 pp.
Parmentier, M., Ollivier, P., Joulian, C., Albrecht, A., Hadi, J., Greneche, J.-M., & Pauwels, H. (2014). Enhanced heterotrophic denitrification in clay media: The role of mineral electron donors. *Chemical Geology*, *390*, 87–99. https://doi.org/10.1016/j.chemgeo.2014.10.014
Pätsch, M. (2006). *Analyse des Depots des Nitratumsatzes und dessen Heterogenität im quartären Grundwasserleiter des Wasserwerks Thülsfelde/Emsland*. TU Dresden: Berücksichtigung bei der Modellierung des Transportes.

Postma, D. (1990). Kinetics of nitrate reduction by detrial Fe (II)-silicates. *Geochimica et Cosmochimica Acta*, *54*(3), 903–908. https://doi.org/10.1016/0016-7037(90)90384-W

Postma, D., Boesen, C., Kristiansen, H., & Larsen, F. (1991). Nitrate reduction in an unconfined sandy aquifer—Water chemistry, reduction processes, and geochemical modeling. *Water Resources Research*, *27*, 2027–2045.

Prommer, H., & Stuyfzand, P. J. (2005). Identification of temperature-dependent water quality changes during a deep well injection experiment in a pyritic aquifer. *Environmental Science & Technology*, *39*(7), 2200–2209. https://doi.org/10.1021/es0486768

Rimstidt, J. D., & Vaughan, D. J. (2003). Pyrite oxidation: A state-of-the-art assessment of the reaction mechanism. *Geochimica et Cosmochimica Acta*, *67*(5), 873–880. https://doi.org/10.1016/S0016-7037(02)01165-1

Rivett, M. O., Buss, S. R., Morgan, P., Smith, J. W. N., & Bemment, C. D. (2008). Nitrate attenuation in groundwater: A review of biogeochemical controlling processes. *Water Research*, *42*(16), 4215–4232. https://doi.org/10.1016/j.watres.2008.07.020

Robertson, W. D., Russell, B. M., & Cherry, J. A. (1996). Attenuation of nitrate in aquitard sediments of southern Ontario. *Journal of Hydrology*, *180*(1–4), 267–281. https://doi.org/10.1016/0022-1694(95)02885-4

Rodríguez-Escales, P., Folch, A., van Breukelen, B. M., Vidal-Gavilan, G., & Sanchez-Vila, X. (2016). Modeling long term enhanced in situ biodenitrification and induced heterogeneity in column experiments under different feeding strategies. *Journal of Hydrology*, *538*, 127–137. https://doi.org/10.1016/j.jhydrol.2016.04.012

Rodríguez-Escales, P., van Breukelen, B. M., Vidal-Gavilan, G., Soler, A., & Folch, A. (2014). Integrated modeling of biogeochemical reactions and associated isotope fractionations at batch scale: A tool to monitor enhanced biodenitrification applications. *Chemical Geology*, *365*, 20–29. https://doi.org/10.1016/j.chemgeo.2013.12.003

Rohmann, U., & Sontheimer, H. (1985). *Nitrat im Grundwasser: Ursachen, Bedeutung, Lösungswege*. Karlsruhe (TH): DVGW-Forschungsstelle am Engler-Bunte-Inst. d. University.

Seal, R. R. (2006). Sulfur isotope geochemistry of sulfide minerals. *Reviews in Mineralogy and Geochemistry*, *61*(1), 633–677. https://doi.org/10.2138/rmg.2006.61.12

Sigman, D. M., Casciotti, K. L., Andreani, M., Barford, C., Galanter, M., & Böhlke, J. K. (2001). A bacterial method for the nitrogen isotopic analysis of nitrate in seawater and freshwater. *Analytical Chemistry*, *73*(17), 4145–4153. https://doi.org/10.1021/ac010088e

Šimůnek, J., van Genuchten, M. T., & Šejna, M. (2016). Recent developments and applications of the HYDRUS computer software packages. *Vadose Zone Journal*, *15*(7). https://doi.org/10.2136/vzj2016.04.0033

Smith, R. L., & Duff, J. H. (1988). Denitrification in a sand and gravel aquifer. *Applied and Environmental Microbiology*, *54*(5), 1071–1078.

Smith, R. L., Garabedian, S. P., & Brooks, M. H. (1996). Comparison of denitrification activity measurements in groundwater using cores and natural-gradient tracer tests. *Environmental Science & Technology*, *30*(12), 3448–3456. https://doi.org/10.1021/es960042g

Starr, R. C., & Gillham, R. W. (1993). Denitrification and organic carbon availability in two aquifers. *Ground Water*, *31*(6), 934–947. https://doi.org/10.1111/j.1745-6584.1993.tb00867.x

Strebel, O., Böttcher, J., & Duynisveld, W. H. M. (1992). Identifizierung und Quantifizierung von Stoffumsetzungen in einem Sand-Aquifer (Beispiel Fuhrberger Feld). *DVGW Schriftenreihe Wasser*, *73*, 55–72.

Strebel, O., Böttcher, J., & Kölle, W. (1985). Stoffbilanzen im Grundwasser eines Einzugsgebietes als Hilfsmittel bei Klärung und Prognose von Grundwasserqualitätsproblemen (Beispiel Fuhrberger Feld). *Z. dt. geol. Ges.*, *136*, 533–541.

Strohm, T. O., Griffin, B., Zumft, W. G., & Schink, B. (2007). Growth yields in bacterial denitrification and nitrate ammonification. *Applied and Environmental Microbiology*, *73*(5), 1420–1424. https://doi.org/10.1128/AEM.02508-06

Stumm, W., & Morgan, J. J. (1996). *Aquatic Chemistry: Chemical Equilibria and Rates in Natural Waters*. New York: Wiley.

Taylor, S. W., & Jaffé, P. R. (1990). Biofilm growth and the related changes in the physical properties of a porous medium: 1. Experimental investigation. *Water Resources Research*, *26*, 2153–2159. https://doi.org/10.1029/WR026i009p02153

Tesoriero, A. J., Liebscher, H., & Cox, S. E. (2000). Mechanism and rate of denitrification in an agricultural watershed: Electron and mass balance along groundwater flow paths. *Water Resources Research*, *36*, 1545–1559. https://doi.org/10.1029/2000WR900035

Tesoriero, A. J., & Puckett, L. J. (2011). O_2 reduction and denitrification rates in shallow aquifers. *Water Resources Research*, *47*, W12522. https://doi.org/10.1029/2011WR010471

Torrentó, C., Urmeneta, J., Otero, N., Soler, A., Viñas, M., & Cama, J. (2011). Enhanced denitrification in groundwater and sediments from a nitrate-contaminated aquifer after addition of pyrite. *Chemical Geology*, *287*(1–2), 90–101. https://doi.org/10.1016/j.chemgeo.2011.06.002

Trudell, M. R., Gillham, R. W., & Cherry, J. A. (1986). An in-situ study of the occurrence and rate of denitrification in a shallow unconfined sand aquifer. *Journal of Hydrology*, *83*(3–4), 251–268. https://doi.org/10.1016/0022-1694(86)90155-1

Tufenkji, N. (2007). Modeling microbial transport in porous media: Traditional approaches and recent developments. *Advances in Water Resources*, *30*(6–7), 1455–1469. https://doi.org/10.1016/j.advwatres.2006.05.014

Vaclavkova, S., Schultz-Jensen, N., Jacobsen, O. S., Elberling, B., & Aamand, J. (2015). Nitrate-controlled anaerobic oxidation of pyrite by *Thiobacillus* cultures. *Geomicrobiology Journal*, *32*(5), 412–419. https://doi.org/10.1080/01490451.2014.940633

van der Veen, A. (2003). Schwefelspeziation und assoziierte Metalle in rezenten Sedimenten, *Gemeinsame Naturwissenschaftliche Fakultät der Technischen Universität Carolo-Wilhelmina zu Braunschweig*.

Vaughan, D. J. (2006). Sulfide mineralogy and geochemistry: Introduction and overview. *Reviews in Mineralogy and Geochemistry*, *61*(1), 1–5. https://doi.org/10.2138/rmg.2006.61.1

Wagman, D. D. (1982). The NBS tables of chemical thermodynamic properties: Selected values for inorganic and C1 and C2 organic substances in SI units, American Chemical Society and the American Institute of Physics for the National Bureau of Standards.

Weston, N. B., & Joye, S. B. (2005). Temperature-driven decoupling of key phases of organic matter degradation in marine sediments. *Proceedings of the National Academy of Sciences of the United States of America*, *102*(47), 17,036–17,040. https://doi.org/10.1073/pnas.0508798102

Wilkin, R. T., & Barnes, H. L. (1997). Formation processes of framboidal pyrite. *Geochimica et Cosmochimica Acta*, *61*(2), 323–339. https://doi.org/10.1016/S0016-7037(96)00320-1

Wilkin, R. T., Barnes, H. L., & Brantley, S. L. (1996). The size distribution of framboidal pyrite in modern sediments: An indicator of redox conditions. *Geochimica et Cosmochimica Acta*, *60*(20), 3897–3912. https://doi.org/10.1016/0016-7037(96)00209-8

Williamson, M. A., & Rimstidt, J. D. (1994). The kinetics and electrochemical rate-determining step of aqueous pyrite oxidation. *Geochimica et Cosmochimica Acta*, *58*(24), 5443–5454. https://doi.org/10.1016/0016-7037(94)90241-0

Wisotzky, F., Leson, M., Böddeker, M., Peterwitz, U., Boes, U., Bretthauer, M., et al. (2011). Nitratabbaukapazität im Grundwasserleiter der Halterner Sande, *bbr*, *06/2011*, 46–52.

Wriedt, G., & Rode, M. (2006). Modelling nitrate transport and turnover in a lowland catchment system. *Journal of Hydrology*, *328*(1–2), 157–176. https://doi.org/10.1016/j.jhydrol.2005.12.017

Wunderlich, A., Meckenstock, R., & Einsiedl, F. (2012). Effect of different carbon substrates on nitrate stable isotope fractionation during microbial denitrification. *Environmental Science & Technology*, *46*(9), 4861–4868. https://doi.org/10.1021/es204075b

Zhang, Y.-C., Slomp, C. P., Broers, H. P., Bostick, B., Passier, H. F., Böttcher, M. E., et al. (2012). Isotopic and microbiological signatures of pyrite-driven denitrification in a sandy aquifer. *Chemical Geology*, *300-301*, 123–132. https://doi.org/10.1016/j.chemgeo.2012.01.024

Zhang, Y. C., Slomp, C. P., Broers, H. P., Passier, H. F., & Van Cappellen, P. (2009). Denitrification coupled to pyrite oxidation and changes in groundwater quality in a shallow sandy aquifer. *Geochimica et Cosmochimica Acta*, *73*(22), 6716–6726. https://doi.org/10.1016/j.gca.2009.08.026